Reverse micelle strategy for effective substitutional Fe-doping in small-sized CeO2 nanocrystals: Assessment of adsorption and photodegradation efficiency of ibuprofen under

Journal Pre-proofs

Reverse micelle strategy for effective substitutional Fe-doping in small-sized CeO_2 nanocrystals: Assessment of adsorption and photodegradation efficiency of ibuprofen under visible light

Olimpia Tammaro, Rosanna Paparo, Marica Chianese, Ida Ritacco, Lucia Caporaso, Matteo Farnesi Camellone, Bruno Masenelli, Anne D. Lamirand, Jean-Marie Bluet, Marco Fontana, Gabriella Pinto, Anna Illiano, Angela Amoresano, Martino Di Serio, Vincenzo Russo, Serena Esposito

PII: S1385-8947(23)06641-X
DOI: https://doi.org/10.1016/j.cej.2023.147909
Reference: CEJ 147909

To appear in: *Chemical Engineering Journal*

Received Date: 18 August 2023
Revised Date: 22 November 2023
Accepted Date: 4 December 2023

Please cite this article as: O. Tammaro, R. Paparo, M. Chianese, I. Ritacco, L. Caporaso, M.F. Camellone, B. Masenelli, A.D. Lamirand, J-M. Bluet, M. Fontana, G. Pinto, A. Illiano, A. Amoresano, M.D. Serio, V. Russo, S. Esposito, Reverse micelle strategy for effective substitutional Fe-doping in small-sized CeO_2 nanocrystals: Assessment of adsorption and photodegradation efficiency of ibuprofen under visible light, *Chemical Engineering Journal* (2023), doi: https://doi.org/10.1016/j.cej.2023.147909

Reverse micelle strategy for effective substitutional Fe-doping in small-sized CeO_2 nanocrystals: assessment of adsorption and photodegradation efficiency of ibuprofen under visible light

Olimpia Tammaro[1,2], Rosanna Paparo[3], Marica Chianese[3], Ida Ritacco[4], Lucia Caporaso[4], Matteo Farnesi Camellone[5], Bruno Masenelli[6], Anne D. Lamirand[6], Jean-Marie Bluet[6], Marco Fontana[1,7], Gabriella Pinto[3], Anna Illiano[3], Angela Amoresano[3], Martino Di Serio[3], Vincenzo Russo[3*], Serena Esposito[1,2*]

[1] Department of Applied Science and Technology and INSTM Unit of Torino – Politecnico, Politecnico di Torino, Corso Duca degli Abruzzi 24, 10129, Torino, Italy

[2] PoliTO BioMED Interdepartmental LAB, Corso Duca degli Abruzzi 24, 10129 Torino, Italy

[3] University of Naples "Federico II", Department of Chemical Sciences, Complesso Universitario Monte S. Angelo, Via Cintia 4, IT 80126 Naples, Italy

[4] Dipartimento di Chimica e Biologia, Università degli Studi di Salerno, via Giovanni Paolo II 132, 84084 Fisciano, Salerno, Italy

[5] Consiglio Nazionale delle Ricerche-Istituto Officina dei Materiali (CNR-IOM), 34136 Trieste, Italy

[6] University of Lyon, INSA Lyon, ECL, CNRS, UCBL, CPE Lyon, INL, UMR5270, 69621 Villeurbanne, France.

[7]Center for Sustainable Future Technologies @POLITO, Istituto Italiano di Tecnologia, Via Livorno 60, Turin 10144, Italy

Corresponding authors: serena_esposito@polito.it; v.russo@unina.it

Abstract

Reverse micelle nanoreactors were successfully designed to synthesize small-sized ceria nanocrystals (3.5-4.2 nm) with a sizeable amount of substitutional iron. Undoped and doped CeO_2 catalysts with an iron content (0.50-10 mol %) compliant with the nominal value were prepared and tested for the first time for the removal of ibuprofen both in the dark and under UV or visible light irradiation.

The effective inclusion and distribution of iron in the ceria lattice were ascertained through in-depth physicochemical characterization. In particular, X-ray diffraction suggested the formation of an F-type crystal structure, ruling out the formation of separate iron-containing crystalline phases. On the other hand, substitutional doping of CeO_2 with Fe atoms favoured the formation of Ce^{3+} defects and vacancy sites (VOs) with a maximum for the sample with 2.5 mol % iron (Fe2.5), as evidenced by X-ray photoelectron spectroscopy (XPS) measurements and Raman spectroscopy. UV-Vis spectroscopy showed that the optical properties were successfully modified by the presence of iron, which causes a gradual decrease in band gap as iron content increases. The experimental evidence was further verified and supported by density functional theory calculations. DFT calculations also revealed that the surface iron and oxygen vacancies are the preferential sites for ibuprofen adsorption. Nevertheless, it was found under dark conditions that adsorption capacity does not monotonically increase with iron content, revealing contrasting roles of surface characteristics. Indeed, catalytic experiments have identified a trade-off between adsorption and photodegradation, identifying Fe2.5 as the best-performing catalyst for ibuprofen removal under visible light irradiation. These results were discussed by considering the key properties of the catalysts as well as their different surface charge determined by ζ potential measurements. The best catalyst was tested through reuse experiments that proved its stability over 4 cycles. Finally, an attempt was made to identify the photodegradation by-products, allowing the detection of 1-ethenyl-4-(2-methylpropyl)benzene as the main by-product.

Keywords: Substitutional Fe doped CeO_2, Reverse micelle, Ibuprofen, Photodegradation, DFT.

1. Introduction

Pharmaceuticals are considered emerging environmental pollutants due to the increase in their consumption and consequent accumulation in water [1]. Ibuprofen (IBU) (Table 1), is among the most widespread non-steroidal anti-inflammatory drugs (NSAIDs) in the world, whose presence in wastewater is a serious concern because it is not biodegradable [2]. The detected concentrations for ibuprofen in wastewater treatment plants are in the ranges of 55–69 $\mu g \cdot L^{-1}$ [3]. Over the last few years, to address this environmental concern, several chemical, physical and biological methods have been proposed [4]. Chemical methods include advanced oxidation processes (AOPs), coagulation-flocculation, electrocoagulation, chemical oxidation, and ion exchange [4]. Among those, AOPs can degrade recalcitrant pollutants with a rapid reaction rate and high removal efficiency due to the generation of reactive free radicals [5].

Table 1 - Structure and properties of ibuprofen

Compound	IUPAC name	Molecular formula	Molecular weight	Solubility in water	Structure
IBU	2-[4-(2-methyl propyl) phenyl]propanoic acid	$C_{13}H_{18}O_2$	206.28 g/mol	21 mg/L (at 25 ºC)	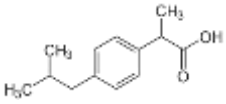

The use of semiconductors has broadened AOPs to heterogeneous photocatalysis, a process operating at room temperature and atmospheric pressure [5–8]. Moreover, the combination, through the design of an appropriate catalyst, with solar reactors makes this method stand out from others in terms of environmental friendliness and cost-effectiveness through the use of renewable energy [9–11]. Indeed, nowadays, new photocatalysts active in the visible range are attracting increasing interest among the scientific community [9].

Although some formulations for the catalytic photodegradation of ibuprofen under visible light were explored, the proposed solutions suffer from the complicated design of the photocatalyst [12–17], and typically the experiments are conducted in harsh reaction conditions (e.g., powerful lamps, highly concentrated systems [14,15]). The challenge is therefore to design simple, inexpensive, high-performance catalysts for optimal degradation of ibuprofen under visible light irradiation.

Cerium oxide was selected for its many trade-offs between reactivity, photochemical stability, cost-effectiveness, and the environmentally friendly nature of CeO_2 nanoparticles (CeO_2-NPs) [18–21].

The photocatalytic activity of cerium oxide can be enhanced, increasing the photo-absorption capability, by replacing a small fraction of Ce^{4+} with a different cation [22,23]. Among heteroatom dopants, transition metals are particularly appealing as they can create defect states in the band gap or introduce energy levels into it. In this regard, iron is considered one of the most attractive candidates on account of its environmental compatibility, abundance, and low cost [24]. One of the most intriguing features of using Fe^{3+} as a dopant is the possibility of further promoting the generation of oxygen vacancies (VOs) and the reversible conversion between the Ce^{4+}/Ce^{3+} valence state. [25,26]. Oxygen vacancies not only extend the absorption edge but are reported to delay the electron–

hole recombination rates, thus increasing the separation efficiency of carriers for enhanced photocatalytic performances [27,28].

In conclusion, the introduction of Fe trivalent ions can be considered a powerful tool for rational defect engineering. Indeed, the beneficial effect of iron doping is reported by a certain number of papers for the photodegradation of model dye molecules under visible irradiation, recently reviewed [22]. Nevertheless, it must be considered that the influence of metal dopant and VOs on the ceria properties is interrelated to the concentration, distribution or position of Fe and defects in the ceria lattice [29]. In particular, the extent to which these features occur can be strongly impacted by the preparation method [30].

In this scenario, it should be noted that many methods reported in the literature suffer from poor reproducibility and control of process parameters, often failing to achieve real doping or, on the other hand, requiring harsh operating conditions [31–36]. The hydrothermal method was exploited by Cai et al. [32] for preparing Fe-doped ceria materials with different doping amounts. They obtained a catalyst with a crystallite size of approximately 100 Å and observed that the low Fe^{3+} doping could effectively improve the concentration of Ce^{3+}, enhancing the degradation ability of the model dye Acid Orange 7 (AO7). However, despite the versatility of the hydrothermal approach, it still represents a “black box” method as is impossible to have strict control over the process. Channei et al. [36] used flame pyrolysis to produce photocatalysts based on Fe-doped CeO_2 nanoparticles for the conversion of both formic acid and oxalic acid. This method, such as the aforementioned hydrothermal method, does not easily allow the control and variation of synthesis parameters invalidating the simplicity of the experimental setup [37].

In this perspective, it is important to have a method that goes beyond the trial-and-error approach and allows rigorous control of the composition of the catalyst, preserving its homogeneity and promoting improved optical, structural, and morphological properties.

Based on the previous considerations, in our work, we bring the reader's attention to a Fe-doped ceria system, so far never adopted for the photodegradation of ibuprofen. A further outcome of this research was the development of a versatile and reliable synthesis protocol, capable of exploiting the recognised advantages and potential of the one-pot reverse micelle approach. From a practical point of view, a significant advantage of the method is its scalability, including synthesis in microfluidic systems, for the production of larger quantities of catalysts [38–44].

The homogeneity of the final material is due to atomic-scale mixing, which in turn is ensured by the presence of a small aqueous core, where the reaction takes place. This mixing allows to easily promote the presence of the dopant in the oxide lattice. The size and shape of these small water domains can be controlled by varying the ratio between the liquid phases (water and oil) and selecting the right surfactant in terms of both type (non-ionic, anionic, cationic and amphoteric) and amount. As a result, not only the intimate contact of the metal precursor is well confined, but also the relative nucleation on growth steps can be easily monitored [45].

A pure ceria and iron-doped ceria with metal contents of 0.5, 2.5, 5 and 10 mol % Fe were prepared channelling the reactions that usually take place in aqueous media into the small domains of the reverse micelles.

To assess the physicochemical properties and to understand the structure/composition-activity relationship of Fe-doped CeO_2 in the photodegradation of ibuprofen, an in-depth characterisation was conducted. In detail, the prepared catalysts were characterised using various analytical techniques such as inductively coupled plasma mass spectrometry (ICP-MS), Thermogravimetric analysis (TGA), X-ray diffraction (XRD), high-resolution transmission electron microscopy (HR-TEM), Field

emission scanning electron microscopy (FESEM), Diffuse reflectance spectroscopy (DR/UV-Vis), Raman spectroscopy, N_2 adsorption/desorption at -196 °C, X-ray photoelectron spectroscopy (XPS) and ζ-potential measurements.

Density Functional Theory (DFT) calculations were performed in order to investigate the stability and the effects on the electronic and structural properties of the CeO_2(111) in the presence of substitutional and interstitial Fe atoms. The calculations suggest that, in a wide range of temperatures and pressure, the thermodynamically most stable structures are the ones where Fe atoms substitute Ce sites in the presence or absence of oxygen vacancies in agreement with the experimental observations. Additional calculations were performed to investigate the interaction between undoped and Fe-doped ceria surfaces with ibuprofen in order to identify preferential sites for adsorption.

The catalysts were tested both in the dark and under either UV or visible irradiation, to compare the performance of each synthesized material. A preliminary kinetic model was implemented to measure the activity of each catalyst in terms of both ibuprofen adsorption and related photodegradation. Reuse experiments were conducted to test the stability of the most active material, further assessed by post-reaction characterizations. Finally, an attempt was made to determine the photodegradation products via specific analytical methods (i.e., GC and LC-MS).

2. Materials and methods

Cyclohexane (ACS reagent ≥ 99.5%), cerium nitrate hexahydrate, iron chloride (reagent grade 97%), ammonia (ACS reagent 28-30%), 1-butanol (ACS reagent ≥ 99.4%), polyoxyethylene (10) cetyl ether (Brij C10) and ethanol (puriss ≥ 99.8%) were purchased by Sigma-Aldrich and used without further modification. Bi-distilled water has been used for the preparation of salt solution. Ibuprofen solutions were prepared using 4-isobutyl-α-methylphenylacetic acid, 99% (manufactured by Alfa Aesar).

2.1 *Precipitation by reverse micelles*

In a typical synthesis, adapted from the literature [46,47], the oil/surfactant phase is prepared by dissolving 8.2 g of surfactant (Brij C10) in 100 mL of cyclohexane under stirring at room temperature. An aqueous solution is prepared by dissolving the proper amount of cerium and iron precursors in distillate water to achieve a final concentration of 0.5M. The volume of the aqueous precursor solution has been selected to obtain a w_0 value of 25 (w_0 is defined as the water-surfactant molar ratio). The aqueous solution is slowly added dropwise to the oil phase to obtain appropriate water-in-oil (w/o) micelles. To preserve the optical transparency of the emulsion, avoiding the formation of flocculates, 4 mL of co-surfactant (1-butanol) are also added. The optimised protocol involves alternating the additions of water and the co-surfactant. Finally, 5.4 mL of precipitating agent, ammonia solution, are slowly dripped. The mixture is stirred for 1.5h at room temperature. The solid phase is then collected by centrifugation, washed twice with ethanol and dried under a hood for 2 days. The dried powder has been manually ground before being calcinated at 120 °C for 6 h. The amounts of cerium and iron were calculated to obtain a nominal composition expressed as a molar % of iron equal to 0 mol % (CeO_2), 0.5 mol % (Fe0.5), 2.5 mol % (Fe2.5), 5 mol% (Fe5) and 10 mol % (Fe10). Samples Fe2.5 after its use as a catalyst for the ibuprofen degradation under visible light was labelled Fe2.5_post reaction.

2.2 *Structural, morphological and surface characterization*

Thermogravimetric analysis was performed on Mettler-Toledo TGA/SDTA 851e instrument. The curves were recorded in air increasing the temperature from 25 to 800 °C at the rate of 10 °C/min.

Inductively coupled plasma mass spectrometry (ICP-MS) analysis (ICAPQ Thermo Scientific) was applied to determine the effective composition of the prepared catalysts, expressed as Fe/Ce molar ratio. Before analysis, samples are subjected to an extraction process with a hot nitric acid solution to ensure complete dissolution of the interest elements. The subsequent dilutions method is used to achieve the concentration range used for calibration curve preparation.

X-ray powder diffraction (XRPD) was performed on a Philips X'Pert diffractometer equipped with a Cu Kα radiation (2θ range = 5° - 90°; step = 0.02° 2θ; time per step = 1 s). Lattice parameters and cell volumes were determined by UnitCell Software, while the crystallite size (L) has been calculated by Scherrer formula: $L = \frac{k\,\lambda}{\beta cos\theta}$, k is a constant equal to 0.90, λ is the X-ray wavelength equal to 0.154 nm, β is the full width at half maximum, and θ is the half diffraction angle.

The optical properties of the powders were recorded on a UV−Vis Varian Cary 5000 spectrophotometer equipped with a DR integration sphere in the 200−600 nm range. The indirect band gap values are obtained by applying the Tauc plot method referring to the formula $(F(R)h\nu)^{1/2} = f(h\nu)$.

The vibrational properties of the samples have been analysed with Raman spectroscopy. Spectra were collected and recorded at room temperature with a LabRAM HR spectrometer (Jobin Yvon-Horiba), using a X50 confocal microscope and an excitation wavelength of 532 nm. The excitation power was kept low to ensure no photodegradation of the samples. The spectra were dispersed with 1800 gr/mm grating, leading to a 1 cm^{-1} accuracy.

Transmission Electron Microscopy characterization was carried out with a Thalos F200X instrument (ThermoFisher) and Energy Dispersive X-ray spectroscopy (EDX) spectra were acquired with four Silicon drift detectors (SDD). The catalysts as dry powders were dispersed in isopropyl alcohol and subsequently drop-casted onto Cu holey carbon grids. Before insertion in the TEM column, the samples were plasma-cleaned in Ar atmosphere. Thermo Scientific Velox software was used for the analysis of TEM and EDX data. The crystallographic model for cubic CeO_2 (Fm-3m space group) is provided in the Crystallography Open Database (COD ID: 4343161). To complete the morphological characterization a field emission scanning electron microscopy (FE-SEM) was used (ZEISS MERLIN instrument (Oberkochen, Germany)).

Textural properties have been evaluated through N_2 physisorption and desorption at 77K (Quantachrome Autosorb1 Instruments.). Before the measurement, the sample was outgassed under a high vacuum at 120°C for 3 hours to remove pollutants previously adsorbed. From the isotherm obtained by nitrogen adsorption, the specific surface area (SSA) of the samples was calculated according to the BET (Brunauer–Emmet–Teller), total pore volume, Vp, was determined from the amount of adsorbed N_2 at p/p°=0.98. BJH pore size distribution was determined by the desorption branch of isotherms [48,49].

X-ray photoelectron spectroscopy (XPS) measurements were carried out in a Prevac spectrometer using a focused monochromatic Al Kα X-ray source (1486.6 eV) with a pass energy of 40 meV for survey scans and 20 meV for detailed scans. Despite our efforts, sample charging occurred and was only partially compensated by an electron flood source. Binding energies were then shifted from one core level to another. To analyse the spectra, the O1s signal was shifted to reach Oα at 529 eV, while

the Ce3d signal referred to as v''' was set at 898.4 eV. Some peak broadening may have resulted from the residual charge. All the peaks were fitted with a Voigt shape function.

ζ-potential curves were obtained by measuring the electrophoretic mobility as a function of pH at 30°C with a Litesizer (Anton Paar Instruments, Worcestershire, UK). The samples were prepared with a starting concentration of 1mg/50mL, and subsequently, 0.1 M NaOH or 0.1 M HCl were added to varying the pH. The ζ-potential measurements were carried out in an Omega cuvette (Anton Paar) accessory. The measurements were performed in triplicate.

FT-IR 4700LE (JASCO, Tokyo, Japan) using the ATR (attenuated total reflectance) was used to obtain Fourier transform infrared (FTIR) spectra, the spectrum was obtained at a resolution of 2 cm^{-1} over the range of 400-4000 cm^{-1}. Firstly, the sample of pristine photocatalyst Fe2.5 was mixed with potassium anhydrous bromide (KBr) (m/m, 1:2000), and the mixture was pressed to obtain a pellet. KBr was used also as reference material. To identify the interaction between IBU and Fe2.5 catalyst, the pellet of Fe2.5 was covered with a drop of saturated IBU solution and dried in an oven at 60°C for one hour before the analysis.

2.3 Computational Details

Density Functional Theory (DFT) calculations were performed within Periodic Boundary Conditions (PBC) using the Perdew-Burke-Ernzerhof (PBE) exchange-correlation functional based on the generalized gradient approximation (GGA) [50] and ultrasoft pseudopotentials [51]. The spin polarized Kohn–Sham equations were solved in the planewave pseudopotential framework, with the wavefunction basis set and the Fourier representation of the charge density being limited by kinetic cutoffs of 60 and 500 Ry, respectively. The Quantum Expresso code [52] was employed for all calculations. It is well established that a reliable description of both stoichiometric and reduced ceria-based materials can be achieved by adding a Hubbard U term to the GGA energy functional acting on the f states of the Ce ions. Therefore, all the calculations reported in this work were performed at the DFT+U level, as implemented by Cococcioni and de Gironcoli [53], employing a U value of 4.5 eV. This is consistent with previous literature reporting values between 4.5 and 5 eV [54–65]. In all calculations the Brillouin zone integration was performed on the Γ point only.

All the calculations were performed on the (111) termination of CeO_2 (Fig. SI.1), being the most stable one and the most present in the experiment (see Fig. 1a). We are aware that this represent a simplification of the system prepared from experiments but from a computational point of view is not possible to capture the complexity of the real system. The Ibuprofen (IBU) molecule is anionic in experimental pH-neutral conditions [66], therefore it was simulated in its deprotonated form when adsorbed on the CeO_2(111) surface. The proton released by the molecule is transferred to O3c (tri-coordinated O) atoms of the surface similarly to previous theoretical studies [67–70].

The CeO_2 (111) surface was modelled using a (5x4) slab supercell with three O-Ce-O trilayers (180 atoms) and separated by more than 20 Å of vacuum in the direction perpendicular to the surface. During the optimizations, the bottom tri-layer of the slab was fixed to simulate the equilibrium bulk-like position, while the upper two tri-layers and the organic ligand were fully relaxed. The O-defective systems were modeled by removing O3c and O4c atoms from the surface and subsurface layers of the CeO_2 (111) slab (VO_x). The formation energies of the oxygen vacancies were computed as $E_{FORM(VO_x)} = E_{VO_x} - E_{CeO_2} + \frac{1}{2}E_{O_2}$, where E_{CeO_2} is the energy of the stoichiometric surface, while E_{VO_x} and E_{O_2} are the energies of the surface with oxygen vacancies and of the gas phase O_2 molecule, respectively.

The adsorption energy of IBU was computed using the formula $E_{ads} = E_{CeO_2/IBU} - (E_{CeO_2} + E_{H-IBU})$, where $E_{CeO_2/IBU}$ is the energy of the combined system (namely the surface plus the anionic IBU), E_{CeO_2} is the energy of the stoichiometric and/or O-defective surface (E_{VOx}) alone, and E_{H-IBU} is the energy of the neutral IBU in gas phase.

The substitutional and interstitial Fe-doping effects were evaluated by replacing and adding Ce atoms in all considered systems.

In order to analyze the thermodynamic stability of different structures in the absence and in the presence of i) Fe dopant and ii) oxygen vacancies as a function of temperature and pressure, the formalism of approximate *ab initio* thermodynamics was employed [71–74]. According to this formalism, the Gibbs energies of the formation of the different ceria systems depend on the temperature and pressure through the following expression (Eq.1):

$$\Delta G_{ads}(T,p) = \frac{1}{A}\{E_{tot} - E_{CeO_2} + N_0^V \mu_0(T,p) + N_{Ce}^V[E_{CeO_2}^{bulk} - 2\mu_0(T,p)] - \mu_{Fe}\} \quad (1)$$

where A is the surface area, E_{tot} and E_{CeO2} are the total energies of the considered ceria system and stoichiometric ceria surface, respectively. The quantities N_O and N_{Ce} represent the number of O and Ce vacancies present in the structure under consideration, whereas $E_{CeO_2}^{bulk}$ is the energy of a formula unit of the CeO_2 bulk phase. Finally, μ_{Fe} and μ_o are the oxygen and iron chemical potentials. The chemical potential of Fe, μ_{Fe}, is set to be the total energy per atom of the bulk Fe crystal, whereas the upper bound of the chemical potential of O_2, $\mu_o(T, p)$, is given by the total energy of molecular oxygen, $\frac{1}{2}E_{O2}$. This upper bound is taken as the zero of our energy scale by using $\Delta\mu_O(T, p) = \mu_o - \frac{1}{2}E_{O2}$. In addition, assuming that volume and entropy contributions are negligible in $\Delta G_{ads}(T, p)$ [73], the Gibbs energies are approximated by the total energies of our DFT calculations.

Electronic properties were investigated only for the most stable systems. In addition, to determine the approximate oxidation states of anions and cations the charge analysis was performed following the Bader's theory since the charge enclosed within the Bader volume can be considered a good approximation of the total electronic charge of an atom [75–77].

2.4 Catalytic and kinetic tests

The photodegradation experiments were conducted in a 1.5 L jacketed glass vessel, closed with a three-neck lid, as reported in Scheme 1. The reactions were carried out using a co-axial lamp, connected to the reactor through the central neck of the lid. In particular, two different lamps were used: a lamp irradiating in the visible region (Sylvania T5, with a power of 4W and a colour temperature of 6500 K, solar emission spectrum, potential difference 220V, and geometry 14 cm x 1.5 cm), or a lamp irradiating in the UV region (Toshiba FL4BLB, with a power of 4W and emission at a wavelength of 365 nm, potential difference 220 V, and geometry 15 cm x 1.5 cm). The irradiance of the lamp in the experimental apparatus was estimated to be 510 W/m^2. One neck of the lid was left free for collecting samples during the reaction, while the last neck is used for measuring the solution temperature through a dedicated thermocouple. The reaction temperature was controlled using an ultra-thermostat while the dispersion agitation was ensured by magnetic stirring. The airflow rate was set through an electronic gas flowmeter regulator (supplied by Bronkhorst). Air dispersion was enhanced by connecting the outlet of the gas flowmeter regulator to a sintered filter of 50 mesh,

immersed in the liquid-solid dispersion. This technical solution allowed it to reach a high gas-liquid surface area, minimizing eventual gas-liquid mass transfer limitations.

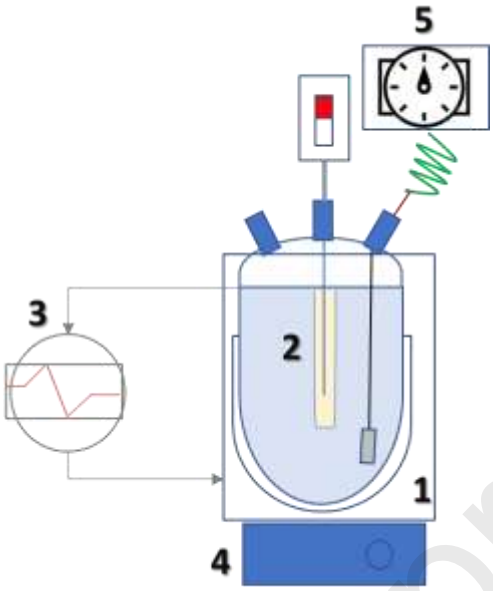

Scheme 1: *Reaction system sketch. 1 Batch reactor, 2 lamps, 3 ultra-thermostat, 4 stirring plates, 5 digital flowmeter regulator.*

As ibuprofen is characterized by relatively low solubility in water (21 mg/L, 25 °C) [78], the solutions (with an initial concentration, $C_{IBU,0}$, of 12.4 mg/L) have been prepared and kept in stirring overnight at room temperature and covered with aluminum foil to protect the solution from the light. After the total dissolution of ibuprofen, the solution is transferred into the reactor, stirred at 750 rpm and warmed up at 30°C. At this point, the catalyst (ρ_B=0.07g/L) was loaded into the reactor. It is important to underline that the operation conditions were chosen from preliminary tests to measure the catalytic activity of the catalysts synthesized in this work.

Three different types of kinetic experiments were conducted: (i) adsorption; (ii) under UV irradiation; (iii) under visible irradiation. In the first case, the system was covered with aluminum foils to prevent any contact with the solution with the solar light. In the other two cases, a specific lamp was adopted as previously stated. Also in the latter cases, the system was covered with aluminum foil. Airflow was adjusted using the digital flow meter and was set at a fixed flow (50mL/min), allowing it to reach full saturation of oxygen in the water. Of course, no air was fed during the adsorption experiments. The reaction was then started by switching on the lamp and prosecuting until a maximum time of 5h.

Before any subsequent operation, a first sample was collected to check the initial ibuprofen concentration ($C_{IBU,0}$); subsequently, samples were collected every 30 minutes for the first 2 hours of reaction, and every hour for the remaining three hours (0, 30, 60, 90, 120, 180, 240 and 300 minutes). Each sample was then centrifuged at 3300 rpm for 30 minutes, and the resulting liquid sample was analyzed by UV-VIS spectroscopy (UV-Vis Jasco V-550), see Supplementary Information for details (Fig. SI.2 and Equation SI-1, i.e., the calibration curve).

2.4.1 Regeneration experiments

The stability of the most active catalyst was tested via reuse experiments, adopting the following reaction conditions: T=30°C, $C_{IBU,0}$=12.4mg/L, ρ_B=0.07 g/L, visible light, Fe2.5 catalyst. In particular, the catalyst was recovered after each photodegradation test, by filtering it on a Buchner funnel. Before reusing it, the catalyst was washed several times on the funnel itself using water, and then was recovered by filtration and oven-dried for 12 h at 60 °C. The procedure was repeated for four cycles [79].

2.4.2 Photodegradation products identification

A dedicated kinetic experiment was performed to identify the reaction products. The experiment was performed using the Fe2.5 catalyst under visible irradiation, adopting an initial concentration of ibuprofen of 12.4 mg/L, a catalyst loading of 0.07 g/L, a stirring rate of 750 rpm, and a temperature of 30 °C.

LC-MS analysis was performed by an Agilent HPLC system (1260 Series) coupled to an Agilent 6230 TOF mass spectrometer apparatus. The HPLC separation was carried out on a reverse-phase C18 column (Poroshell 120 EC-C18 3x50 mm 2.7 um from Agilent Life Sciences) by using water and acetonitrile as mobile phases A and B, respectively, both acidified with 0.1% formic acid. A linear gradient was employed by increasing mobile phase B from 50% to 95% over 9 min at a flow rate of 0.3 mL min^{-1}. The injection volume of each sample was 20 µL and the MS source was an electrospray ionization (ESI) interface in the positive ion mode with a capillary voltage of 3000 V, gas temperature at 325 °C, dry gas (N_2) flow at 5 L min^{-1} and the nebulizer pressure at 35 psi, the fragment at 50 V. The MS spectra were acquired in a mass range of 50–1000 m/z with a rate of 1 spectrum/s, abundance threshold 200 (0.015 relative thresholds).

GC-MS analyses were performed on a 5390 MSD quadrupole mass spectrometer (Agilent Technologies) equipped with a gas chromatograph by using a Polysiloxane DB-5 column ((5%-Phenyl)-methylpolysiloxane, Agilent Technologies) (30m x 0.25 mm x 0.25 µm) from Phenomenex. The injection temperature was 250°C, the oven temperature was increased and held at 50°C for three minutes and then increased to 150°C at 10°C/min, increasing to 230°C at 14 °C/min and finally to 280 °C at 15 °C/min held for 7 min. Electron Ionization mass spectra were recorded by continuous quadrupole scanning at 70 eV ionization energy, in the mass range of m/z 40-550 analysis. Each sample was measured in triplicate.

3. Results and discussion

3.1 *About the adopted reverse micelle approach*

Although the co-precipitation-based synthesis method is extensively used, with a very simple set-up, it suffers from poor control over particle size and homogeneity in mixed oxide systems [80].

In this work, the aforementioned drawbacks were overcome by channelling the reactions that normally take place in aqueous media into the small domains of reverse micelles. Specifically, an aqueous solution containing the iron and cerium precursor was added to a solution of the non-ionic

surfactant, Brij C10, in cyclohexane, generating a water-oil microemulsion. The cage-like environment provided by the microemulsion with the simultaneous presence of the cerium and iron precursors, enabled excellent control of the final stoichiometry, resulting in homogeneity and mixing on an atomic scale, ultimately favouring the effective inclusion of iron heteroatoms in large amounts, as discussed hereafter [80–84].

The synthesis parameters, in particular the type and nature of the surfactant and the water/surfactant ratio, were optimized after careful variation. The value *w*, defined as the water-surfactant molar ratio ([H_2O/BrijC10]), is considered a key parameter for tuning the size of the spherical droplet, affecting the dynamics of water and defining the spatial confinement of the reaction [85,86]. The occurrence of chemical reactions was clearly visible through the colour change of the macrosystem, which moved from a colourless/pale yellow to purple-dense, turning yellow after the fixed reaction time (estimated at one and a half hours). The formation of the purple slurry was attributed to the generation of insoluble Ce^{3+} species that after the complete oxidation turned to yellow Ce^{4+} species [46,87]. The obtained material was recovered by centrifugation, washed to purify from the oil/surfactant, and left catalysts to dry under the hood. Then, the dried powders were heat treated at 120 °C for 6h. The absence of significant quantities of organic residues, confirming the effectiveness of the protocol without the need to use high calcination temperatures, was revealed by the thermogravimetric analysis (Fig. SI.3). The thermal behaviour of the material was explained by identifying three regions in the thermogravimetric curve: (i) from room temperature to 120 °C where the weight loss is due to physisorbed water, (ii) 200-350 °C related to the removal of chemisorbed water occurs, (iii) 400-800 °C characteristic of combustion of organic compounds [88–90]. The synthesis procedure was designed to ensure the highest reproducibility. The effective presence of iron species into the ceria phase was highlighted by the different colour of the powders, changing from light yellow for pure ceria to a reddish-yellow with increasing in the Fe contents (Fig. SI.4).

The results of the quantitative analysis performed by ICP-MS are shown in Table 2. The Fe/Ce ratio is in excellent agreement with the nominal value, showing that the adopted synthesis protocol effectively preserves stoichiometry and avoids material losses during the production steps.

3.2 *Structural, textural and surface properties*

Cerium oxide occurs in the fluorite phase where the cerium atoms are organised in a face-centered cubic lattice structure with 8-fold coordination, while the oxygens are present as OCe4 units [91]. Defect chemistry and the numerous studies conducted on doped and undoped nanometric CeO_2 crystal structure have unequivocally stated that its reactivity and performance of heterogeneous catalysis are surprisingly modulable by engineering the defects and surface structure using a flexible and reliable synthesis procedure [92,93].

XRD diffraction patterns of ceria and Fe-containing ceria samples are reported in Fig. 1a. The pristine ceria shows an XRD profile corresponding to a cubic fluorite structure (JCPDS files 34-0394), where the peak at 28.5°, 33.3°, 47.1° and 56.1° can be associated with the planes 111, 200, 220, and 311, respectively [46]. Although the diffraction patterns of Fe-containing samples reveal that the F-type crystalline structure is retained, the diffraction lines show a progressive shift towards higher 2-teta values, Fig. 1b [46]. As reported by many authors, an isomorphic substitution of Ce^{4+} ions (ionic radius 0.97 Å, coordination number CN=8) by smaller Fe^{3+} ions (ionic radius 0.78Å, CN=8) can account for the lattice shrinkage, appearing as a displacement of the diffraction patterns towards higher angles [25,93]. The observed lattice constraint follows Vegard's law [94] as suggested by the lattice parameters reported in Table 2 and further evidenced by Fig. SI.5. Substitutional doping with the formation of oxygen vacancies, one oxygen vacancy paired with two M^{3+} for charge

neutrality, is a dominant mechanism for ceria doped with aliovalent cations [93,95]. Nevertheless, the small size of Fe^{3+} also allows for a dopant interstitial compensation mechanism where three Fe^{3+} in substitution sites are coupled to one in interstitial sites. This last mechanism leads to a decrease in oxygen vacancy concentration. The further increase in iron content may subsequently promote epitaxial growth on the CeO_2 surface [25,96]. In this scenario, the adopted synthesis method was decisive in promoting substitutional doping, limiting the formation of crystalline phases attributable to iron oxides. The type of doping was also supported by DFT calculation (*vide infra*).

Moreover, the control exerted by the aqueous core during synthesis is successfully reflected in the formation of small-sized crystallites (Table 2), compared to the more conventional methods [96–98]

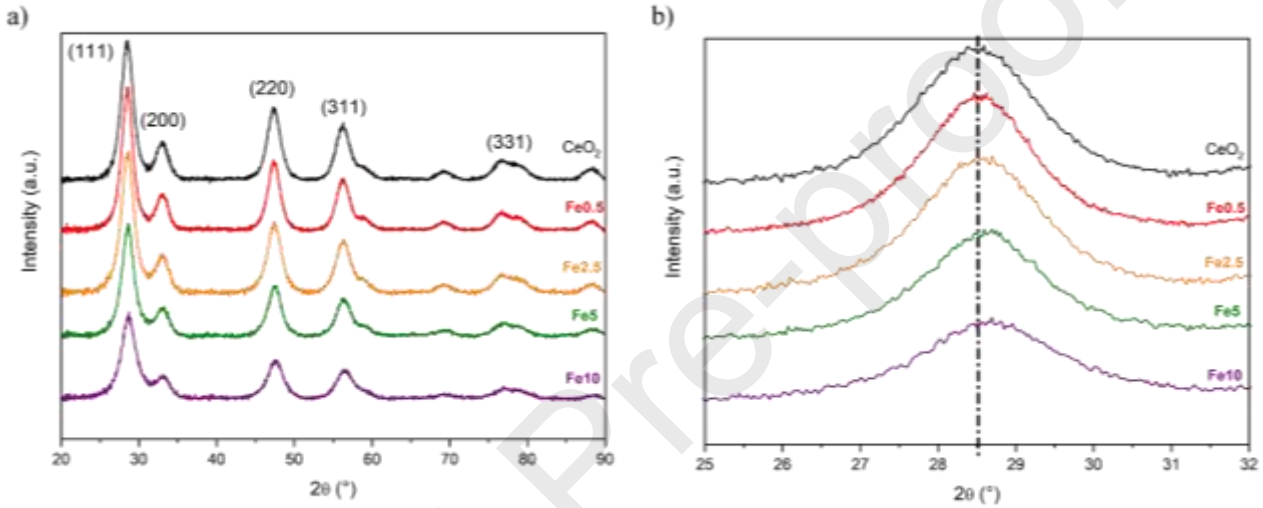

Fig. 1: a) XRD patterns of the synthetized samples in 2theta range 20°-90° and b) enlarged view of (111) diffraction peak.

Table 2: Summary of analytical data: chemical composition calculated from ICP-MS elemental analysis and structural parameters obtained from the cell refinement of the XRD patterns.

Sample	Nominal ratio Fe/Ce (molar %)	Actual ratio Fe/Ce ICP-MS (molar %)	Lattice Parameter (Å)[a]	Cell Volume (Å^3)	Crystallite size, L (Å)[b]
CeO_2	-	-	5.4269± 3 *10^{-4}	159.83± 2 *10^{-2}	42

Fe0.5	0.5	0.66	5.4259± 3 *10^{-4}	159.74± 2 *10^{-2}	44
Fe2.5	2.58	2.87	5.4234± 3 *10^{-4}	159.52± 2 *10^{-2}	40
Fe5	5.31	4.3	5.4162± 3 *10^{-4}	158.89± 2 *10^{-2}	40
Fe10	11.2	11.1	5.4030± 3 *10^{-4}	157.72± 2 *10^{-2}	34

[a] for fluorite phase; [b] Calculated using Scherrer equation due to (1 1 1) plane

Further insight into the morphology and structure of the iron-doped ceria catalysts is provided by Transmission and Scanning Electron Microscopy (Fig. 2 and Fig.SI.6, respectively). Based on TEM images (Fig. 2a), the catalyst powders are constituted of aggregates of approximately spherical nanoparticles. Inspection of high-resolution images reveals that the nanoparticles are single crystalline, with a crystalline structure corresponding to cubic CeO_2 (Fm-3m space group). It is worth pointing out that the characteristic size of the nanoparticles is in the order of 5 nm or lower, in accordance with the crystallite size estimation based on the application of the Scherrer formula on XRD data.

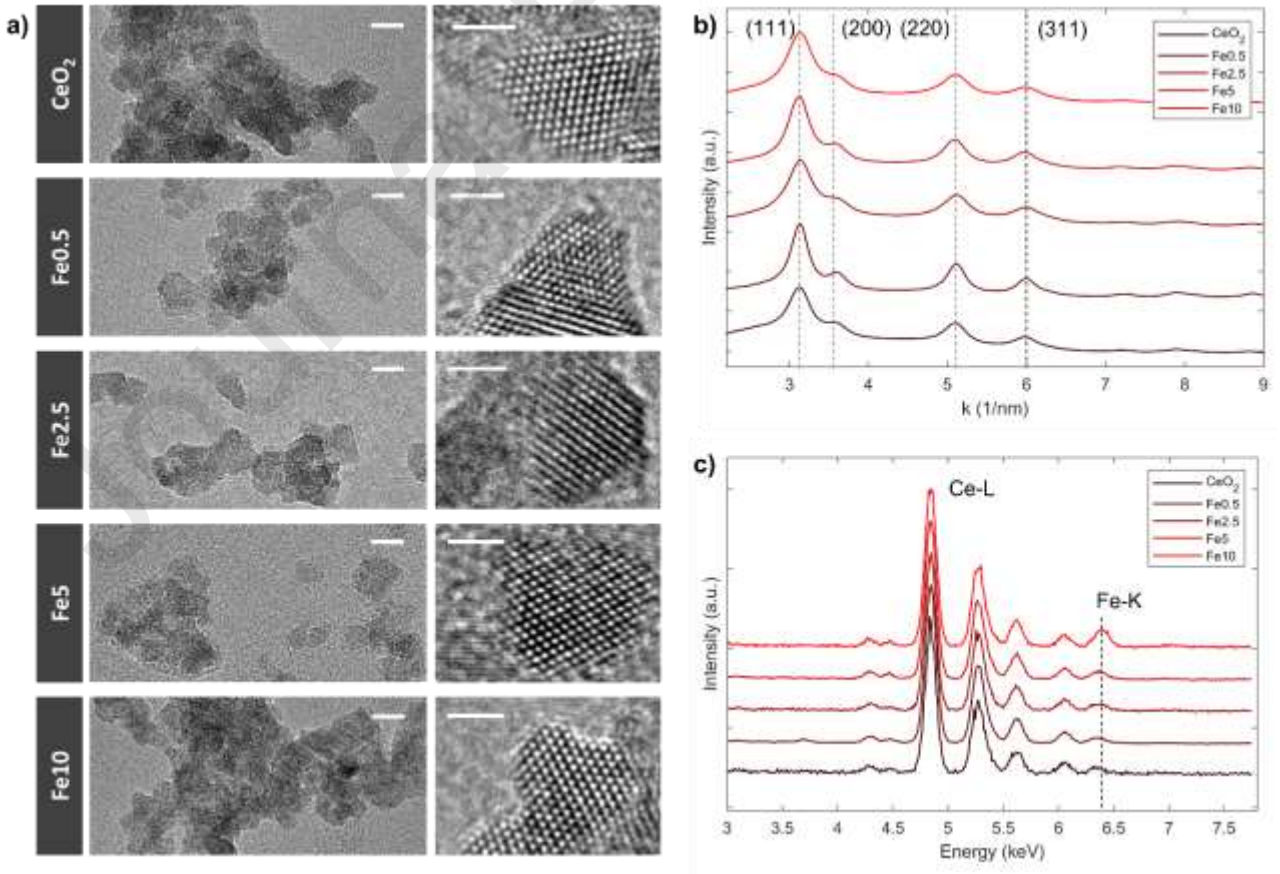

Fig. 2: a) TEM high-resolution images of the different Fe-doped CeO_2 catalysts (scalebar: left column 5 nm, right column 2 nm). Rotationally-averaged selected-area electron diffraction patterns are provided in b). Representative EDX spectra are shown in c).

Moreover, from high-resolution images, there is no evidence of secondary iron-containing crystalline phases. This is confirmed by rotationally-averaged selected area electron diffraction (SAED) patterns, such as the ones provided in Fig. 2b. For each Fe-containing catalyst sample, the diffraction patterns only show peaks corresponding to the (111), (200), (220), and (311) family of crystallographic planes of cubic CeO_2, in agreement with the previously discussed XRD results. Finally, EDX spectra of the catalysts (Fig. 2c) indicate the presence of Fe in all the samples besides pristine CeO_2. It is interesting to notice that the contribution from the Fe Kα line (~ 6.4 keV) in EDX spectra correlates with the nominal increase of Fe in the catalysts, confirming that the crystalline nanoparticles host an increasing amount of Fe ions, without significant changes in the F-type crystalline structure of CeO_2. The SEM micrographs (Fig.SI.6) show a quasi-spherical shape of nanoparticles with a uniform distribution, in agreement with the morphologies obtained from TEM data. To further confirm the presence of Fe in all samples a compositional analysis has been done also by EDS. The atomic ratio Fe/Ce obtained (average in 5 spots) is in good accordance with the theoretical molar ratio and experimental ICP data (see Table SI.1 for details). The optical properties of the prepared materials were evaluated by UV-Vis diffuse reflectance spectroscopy. The D(R) spectra are shown in Fig. 3a. The UV-Vis spectrum of pure CeO_2, black line, consisted of a strong absorption band located in the 200-400 nm range where different transitions can be observed. The absorption at low wavelength, one centered at 215 nm and the other at around 275 nm (blue rectangle and green rectangle in Fig. 3a, respectively), are generally attributed to charge-transfer transitions between O 2p and Ce 4f orbital. In particular, the absorption due to $Ce^{3+} \leftarrow O^{2-}$ charge transfer is observed at 215 nm while the peak at a higher wavelength is ascribed to $Ce^{4+} \leftarrow O^{2-}$ transition [97,99]. The shoulder at 340 nm is assigned to interband transitions [46]. The reported behaviour is also observed in the spectra of iron-containing samples; however, a careful examination reveals some modifications.

The shift to the lower wave number of the main peak recorded for the Fe0.5 sample could be caused by the isolated Fe^{3+} species[100,101]. Indeed, Fe Oh and Td species show the typical transitions in the UV range, allowing a not easy assignment due to overlapping absorption range with ceria. The absorption at 215 nm appears more prominent when increasing the iron doping percentage up to Fe2.5, thus suggesting a more pronounced presence of defective sites [102]. The spectrum recorded for the Fe10 sample (purple curve) shows a feature at about 380 nm that is generally assigned to the presence of oligomeric hematite-like clusters, as reported by Schwidder et al [42]. However, the typical d-d transitions of α-Fe_2O_3, located at 533 nm, are not observed. The lack of stoichiometric iron phase is in accordance with the XRD results, whereas the oligomeric clusters are in accordance with the Raman results, which evidence a contribution at (~ 670 cm^{-1}) only into the sample at higher iron loading (*vide infra)*. The spectra of all the iron-doped catalysts show a red shift in the absorption edge, indicative of the Ce–Fe interaction.

The effect of iron doping on the optical band gap was assessed by Tauc plot relation. In Fig. 3b $(F(R)(h\nu)^{\wedge 1/2})$ is plotted versus the photon energy, hν, and the indirect band gap energy (Eg) was obtained by applying the double tan approximation [103]. The band gap value of pristine CeO_2 was found to be 3.0 eV. The effective inclusion of the Fe species in the ceria lattice results in a decrease in Eg, ascribable to the introduction of vacant 3d orbitals between the valence and conduction bands of CeO_2 [104].

Table 3 shows that Eg values decrease monotonically with iron content [36,60]. This trend is also observed in the theoretical Eg values calculated for the undoped and Fe-doped CeO_2 discussed in the following DFT study section. The band gap values obtained in the iron-doped samples reported here are somewhat lower than those reported in the literature for the same compositions [36,60,105–107]. Once again, all the previous features can be attributed to the adopted reverse micelle strategies.

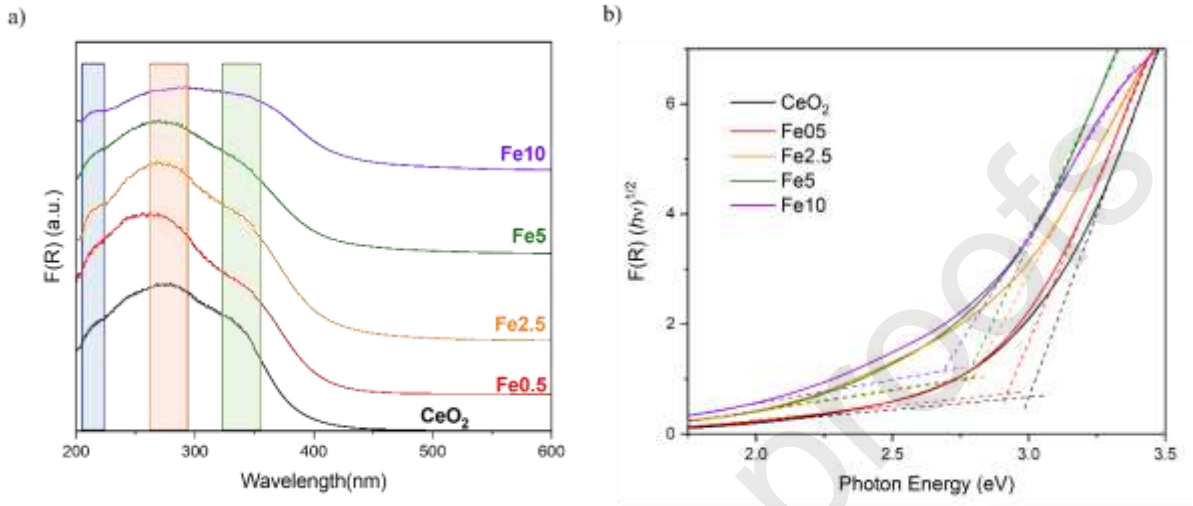

Fig. 3: a) DR UV−Vis spectra of synthetized samples plotted as Kubelka- Munk function F(R). b) The indirect band gap calculation of pristine and Fe-doped porous CeO_2 based on the Kubelka-Munk function by Tauc plot relation using the double tan approximation. CeO_2 (black curve); Fe0.5 (red curve), Fe2.5 (orange curve), Fe5 (green curve) and Fe10 (purple curve).

Significant information on the fate of iron in ceria nanocrystals can be obtained from Raman. The spectra corresponding to the iron-doped samples are shown in Fig. 4a along with that of pure CeO_2 nanocrystals. Three main contributions are observed. The prominent peak corresponds to the F_{2g} peak and it results from the vibration of the O sublattice. It stands at 458.5 cm^{-1} for the pure CeO_2 nanocrystals, some 6.5 cm^{-1} lower than the position of pristine bulk CeO_2. This shift is consistent with the reported decrease of peak position with particle size reduction [91] and a Gruneisen parameter value of 1.57. For instance, Spanier et al. [108] reported a 4 cm^{-1} redshift for 6 nm nanocrystals. The peak shows an asymmetry towards low wavenumbers. Such an asymmetry is often seen in nanocrystal samples and related to size dispersion [91,109,110].

As iron is incorporated into the nanocrystals, the F_{2g} peak mode is further softened and broadened. Such behaviour was previously observed by Popovic et al. [111] for Fe-doped CeO_2 nanocrystals. The trend is not strictly monotonous with the nominal Fe concentration. Fig. 4b shows the correlation between the F_{2g} peak shift ($\Delta\omega$) and the corresponding variation of the peak FWHM (full-width-at-half-maximum). The variation is linear as previously observed by Popovic et al. However, the slope of our curve is -6.9, slightly higher than that reported in [111], with a value of -5.3. This behaviour originates from two causes: grain size and strain effect (causing homogeneous line broadening) and charges delocalization in oxygen-deficient ceria. Since all the samples have about the same nanocrystal mean size, neither the mode softening nor the line broadening can be attributed to any size effect. The observed linear variation thus results from changes in strain within the nanocrystals and charge delocalization. The two phenomena are hard to disentangle without further modelling.

However, the actual occurrence of such a variation is the signature that the samples are oxygen deficient and that charge delocalization happens for 4f electrons located at Ce(Fe)-VO-Ce(Fe) orbitals. This charge delocalization is generally favourable to the photocatalytic activity. This is confirmed in our case where the sample Fe2.5 shows both the highest delocalization and the highest photocatalytic activity (see Fig. 11). We exclude from our analysis the Fe10 sample that cannot be considered as simply doped ceria since it probably contains oligomeric species at its surface, detrimental to its catalytic activity.

Two supplementary peaks are noticed at 270 cm^{-1} and 606 cm^{-1} respectively. They are assigned to the F_{1TO} and F_{1LO} phonon modes. These vibrations are forbidden in pristine CeO_2 but are often seen in nanocrystal samples as a result of the long-range symmetry breaking of the crystals. The magnitude of the F_{1LO} peak increases with Fe content as evidenced in Fig. SI.7 where the change in the ratio between the F1LO contribution and the F2g contribution is plotted versus the sample composition. The F_{1LO} feature can be assigned to defects involving dopant cation complexes close to VO [112]. It can be clearly observed that moving from sample Fe0.5 to sample Fe2.5 the ratio is almost doubled, indicating the increased presence of the aforementioned VO-related complexes.

For the Fe10 sample, on top of the F_{1LO} feature, a second contribution at approximately 670 cm^{-1} appears. This contribution cannot be assigned to the presence of VO but rather to the presence of Fe at high content [112]. As already mentioned, this sample cannot be considered in the strict sense as doped ceria.

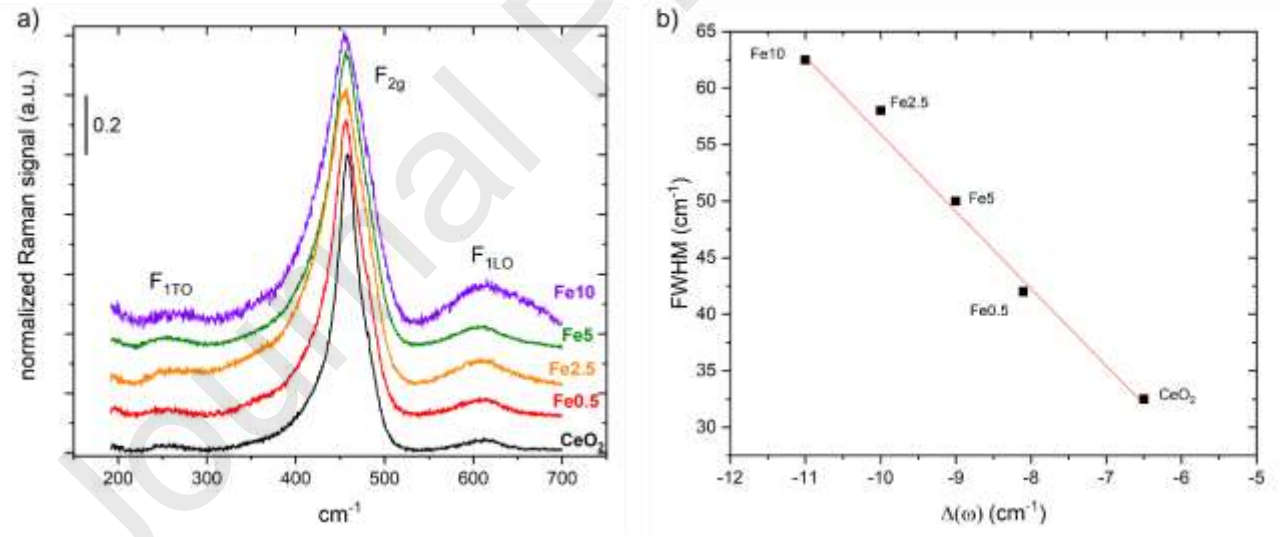

Fig. 4: a) Raman spectra of pristine and Fe-doped CeO_2 nanocrystals for different doping concentrations. All spectra are normalized to the maximum intensity of the F_{2g} peak. b) Variation of the F_{2g} peak FWHM concerning its position variation as a function of the Fe concentration in CeO_2 nanocrystals. $\Delta\omega$ is referred to the value of pristine CeO_2.

The textural properties were evaluated by N_2 adsorption at low temperatures (-196 °C). The adsorption/desorption isotherms, Fig. SI.8a, resemble type IV, typical of mesoporous material with a hysteresis loop indicating block-neck pores shape (hysteresis type H2). All the studied samples have

a BET-specific surface area higher than or equal to 180 $m^2 g^{-1}$ Table 3, with the exception of the sample Fe10 that shows a surface area of 274 $m^2 g^{-1}$. Considering that the surface area is interparticle, the discordant value of Fe10 can be explained by the smaller particle size, Table 2. The limited particle growth observed at high iron contents may be correlated with the presence of iron-containing species on the surface [46,93]. The pore size distribution (PSD) evaluated by the BJH method on desorption branches, Fig.SI.8b, suggests that the synthetic route is effective for the preparation of mesoporous (doped) ceria.

The designed reverse micelles synthesis route allows for obtaining a very high surface area compared, not only with different methods [33,107,113] but also with similar procedures reported in the literature [46,47].

Table 3: Energy of band gap (Eg) and textural properties of pristine and Fe-doped CeO_2 sample

Sample	Eg (eV)	BET SSA ($m^2 g^{-1}$)	Vp ($cm^3 g^{-1}$)
CeO_2	3.00	182	0.196
Fe0.5	2.91	180	0.184
Fe2.5	2.79	191	0.188
Fe5	2.77	189	0.192
Fe10	2.68	274	0.280

In order to have a better comprehension of materials surface a XPS analysis was conducted. Ce3d XPS spectrum, although highly complex, can be deconvolved with some precautions [114,115]. Here Ce3d XPS spectra, shown in Fig. 5a, were solved with five $3d_{5/2}$ components denoted as v_0 (880.6 eV), v (882.6 eV), v'(885.45 eV), v''(888.85 eV) and v'''(898.4 eV) with +/- 0.3 eV resolution and their $3d_{3/2}$ counterparts (called u_x) separated by 18.45 eV (+/-0.15 eV) with a ratio u_x/v_x of 1.5(+/-0.1). The amount of surface Ce^{3+} ion was determined using the area of v0, u0, v' and u' peaks, while v, u, v'', u'', v''' and u''' were assigned to surface Ce^{4+} ion.

The two ions appear for different environments of Ce atoms, resulting in different charge transfers. Ce^{3+} is indeed present in Ce_2O_3, while CeO_2 is made of Ce^{4+} ions. Since the O1s core level is sensitive to changes in the coordination of the oxygen atoms, its deconvolution should also allow the evaluation of the charge transfer between oxygen and cerium atoms. Three components are usually considered to resolve XPS spectra of the O1s core level in CeO_2. The first one, labeled Oα at 529 eV, is usually associated with lattice oxygen, i.e. Ce^{4+} in CeO_2. Following [116], Oβ feature at 531 eV and Oγ feature at 532 eV are attributed to surface hydroxyl groups, resulting from the dissociation of adsorbed water and irreversibly adsorbed molecular water, respectively. These energies (+/-0.1 eV) were fixed to fit our XPS data, as shown in Fig. 5b. Finally, relative atomic concentration was

calculated as the ratio of the normalized intensity of one element with a given valence over the normalized intensity of that element (whatever the valence), with a sensitivity factor calculated as the product of theoretical inelastic mean free path and cross section.

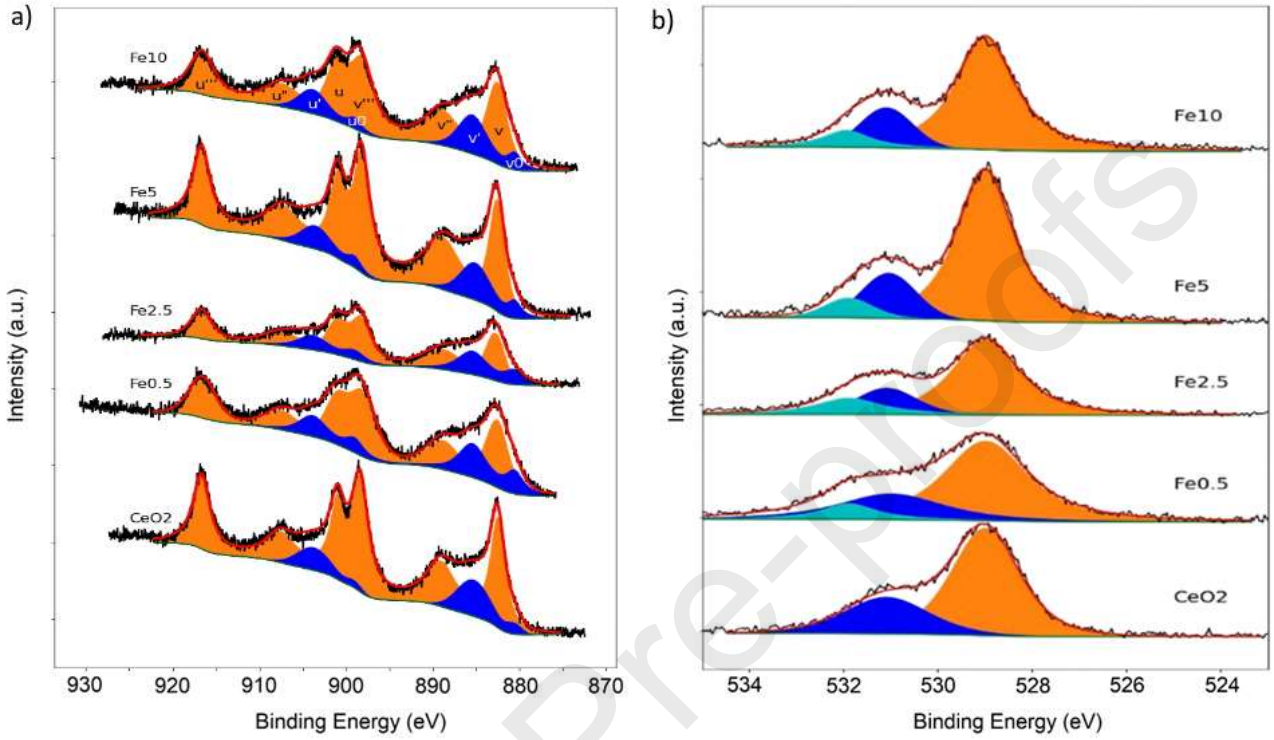

Fig. 5: Experimental and fitted XPS spectra. Ce3d (a) and O1s (b) core level spectra as a function of the Fe concentration in CeO2 nanocrystals. Experimental data are in black, shirley background in green. The sum of 5 components of doublets (2 of Ce^{3+}, blue area, 3 of Ce4+, orange area) are used to fit the Ce3d signal (a) or of 3 components (Oα, Oβ and Oγ, areas in orange, blue and cyan, respectively) to fit O1s signal in red.

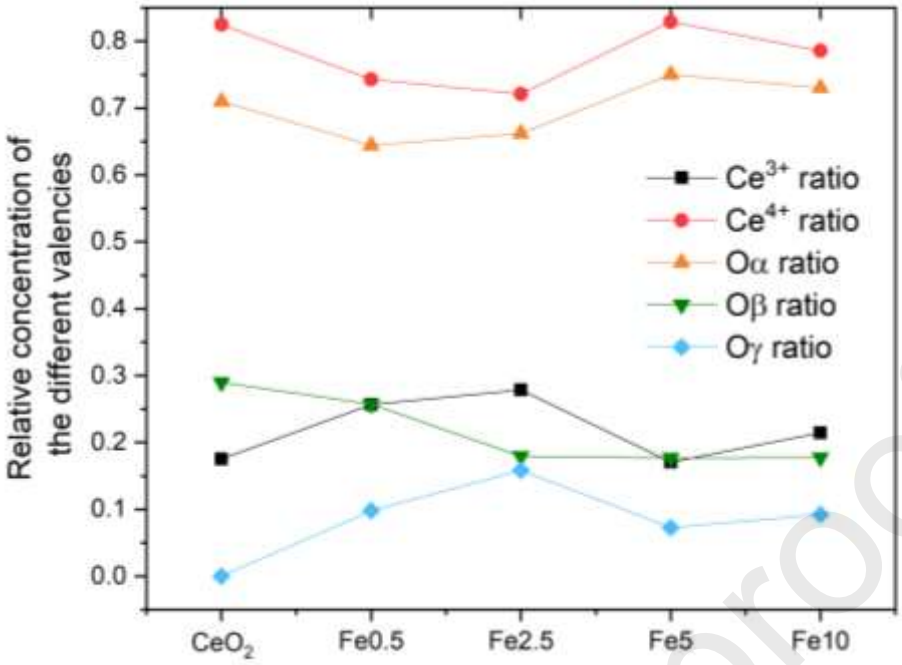

Fig. 6: Relative atomic composition of the synthetized pristine and doped CeO_2 nanocrystals as a function of Fe content.

As shown in Fig. 6, the Ce^{4+} relative atomic concentration follows nicely that of Oα. Both signals decrease as the Fe content increases from CeO_2 to Fe2.5 and next decrease and reach an almost constant value. This is consistent since both signals come from the CeO_2 units in the nanocrystal bulk. Remarkably, the variation of the Ce^{3+} relative atomic concentration is opposite to that of Ce^{4+}. This reveals that the increase in Fe content from CeO_2 to Fe2.5 promotes the enrichment of Ce^{3+} within the Ce. Adding more Fe does not lead to more Ce^{3+} ions. On the contrary, it appears that the further addition of Fe atoms, beyond Fe2.5, is less effective in generating Ce^{3+} ions.

As demonstrated by DFT calculations (see below), the generation of Ce^{3+} ions is related to the generation of VOs The evolution of the oxygen concentration cannot be directly seen in the XPS spectra since, as stated above, there is no XPS feature directly related to VOs. Consequently, even though the analysis of the Ce^{3+} feature remains delicate since the X rays may induce the reduction of ceria during the observation [117], its evolution remains a relevant indication of the VOs concentration. Interestingly, one can note that the minimum Ce^{4+} concentration (thus the maximum of Ce^{3+} and VOs concentrations) is concomitant with the maximum catalytic activity.

To conclude the discussion, the analysis of the Fe2p core level signal would have been highly relevant. However, Fe2p signal is very weak, although increasing with doping, and at the same energies as the signal of Ce M45N45V Auger electrons (see supplementary Fig. SI.9). From its analysis only 3% atomic concentration was found when 10% was expected. As XPS is sensitive to the extreme surface (first few nms), it indicates that Fe might be inhomogeneously distributed in the nanocrystals.

3.3 DFT study

633

634 *3.3.1. Fe-doped CeO_2 surfaces characterization*

635 Density functional theory (DFT) calculations were performed to investigate the effects of Fe-doping
636 on the structural and electronic properties of CeO_2 (111) surfaces. We have considered the scenario
637 in which iron atoms substitute surface and subsurface Ce sites (Fe@Ce) as well as interstitial doping,
638 where Fe atoms occupy interstitial sites in the crystal structure (Fe_{Int}).

639 The optimized geometry of the system with surface substitutional Fe doping ($Fe@Ce_1$), reported in
640 Fig. 7a, results in more stable than the subsurface one ($Fe@Ce_2$) by 1.1 eV. The presence of such a
641 Fe substitutional point defect induces a rearrangement of the neighboring O atoms. As a result, on the
642 doped CeO_2 (111) surface, two non-equivalent O atoms (O_1 and O_4) and two equivalent (O_2=O_3) O
643 sites are present, whereas in the subsurface layer all the O atoms (O_5, O_6 and O_7) results to be
644 equivalent (see Fig. 7b). In this configuration, the Fe atom relaxes inward and binds to an O atom of
645 the surface O_1, to three O atoms of the second layer O_5, O_6 and O_7, and to an O atom of the third layer
646 O_8 (yellow O in Fig. 7b). The Fe-O bond lengths are found to be in the range of 1.84-2.14 Å, and
647 therefore, corresponding to the distances in α- and γ-Fe_2O_3 (1.89-2.10 Å) [118]. In addition, the Bader
648 charge of the substitutional Fe dopant is 14.28 e^- similar to those computed for the metal in α- and γ-
649 Fe_2O_3 (14.34 and 14.49 e^-). The Fe-O bond lengths of the five-coordinate moiety and the Bader charge
650 calculations suggest that in our system the iron atom has an oxidation state of +3. In the doped surface,
651 the Bader charges of the Ce atoms (9.6 e^-) are consistent with the presence of Ce^{4+}, indicating that no
652 Ce^{4+} is reduced to Ce^{3+} in presence of the Fe dopant (see PDOS Fig. SI.10a). In the presence of a
653 substitutional Fe atom in the CeO_2 system the computed value of the bandgap is 1.7 eV, thus 0.2 eV
654 lower with respect to the undoped case, that is 1.9 eV (compare Fig. SI.10a and SI.10b).

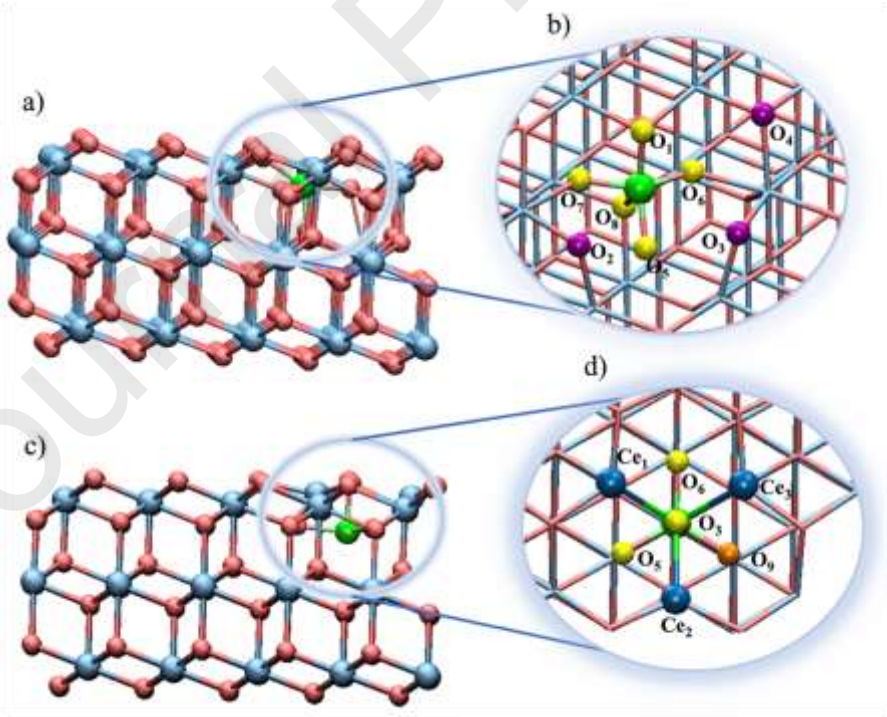

655

656 **Fig. 7**. Panel a) optimized structure of $Fe@Ce_1$ (111). Panel b) First and second coordination spheres
657 of the Fe dopant. Ce, O, $O_{1,5-8}$, O_{2-4} and Fe surface atoms are represented in balls and sticks and
658 depicted in blue, red, yellow, purple and green, respectively. Panel c) optimized structure of Fe_{Int}.

Panel d) coordination sphere of the interstitial Fe dopant. Ce, O, $O_{3,5,6}$, O_9 and Fe surface atoms are represented in balls and sticks and depicted in blue, red, yellow, orange, and green, respectively.

Fig. 7.c shows the optimized structure of the Fe_{Int} system. Also in this case, the presence of the interstitial Fe dopant induces structural distortions on the surface. In fact, the Fe atom relaxes outward binding to the surface O_3 atoms and to the three O atoms of the second layer O_5, O_6 and O_9, (yellow and orange O in Fig. 7d). The formation of these new Fe-O bonds and the breaking of the pre-existing Ce-O bonds generates three reduced Ce^{3+}. The Bader charges of these Ce atoms (9.9 e^-) are consistent with the presence of Ce^{3+}, also confirmed by the formation of two bandgap states below the Fermi level (black peaks in Fig. SI.11a of the SI) and by the spin density analysis, where the electron excess on the Ce^{3+} are indicated with black densities analogously to the colors of the respective bandgap peaks (Fig. SI.11c). In Fe_{Int} system the computed value of the bandgap is 1.7 eV similar to the substitutional Fe doping (compare Fig. SI.10a and SI.11a). For both doping types, the theoretical $\Delta\Delta E$ (eV) related to the band gap energy variation of the undoped and doped surfaces is in line with the experimentally calculated one and reported in Table 3.

Next, we have considered the formation of O vacancies on the most stable $Fe@Ce_1$ system. The presence of a Fe substitutional point defect generates four non-equivalent O atoms, namely O_1, O_2=O_3, O_4 in the outermost layer and O_5=O_6=O_7 in the subsurface layer, as discussed above (Fig. 7b). It is, therefore, possible to create four non-equivalent oxygen vacancies: VO_1, $VO_{2=3}$ and VO_4 in the external layer and $VO_{5=6=7}$ in the subsurface layer. The computed values of the formation energies (E_F) of VO_1, $VO_{2=3}$, VO_4 and $VO_{5=6=7}$ are found to be 0.7, 0.8, 2.13 and 1.1 eV, respectively. Our results show low formation energies for those oxygen vacancies arising from oxygen atoms directly coordinating or close enough to the Fe dopant (see VO_1, $VO_{2=3}$ and $VO_{5=6=7}$) and high E_F for those far from the iron atom. This occurs because the oxygen atoms very close to Fe are more affected by the structural distortions generated by the Fe dopant. The formation of a second oxygen vacancy VO_2 on the most stable reduced surface VO_1 ($Fe@Ce_1$:$VO_{1\text{-}2}$) is also favored, with an E_F of 0.9 eV, suggesting that the Fe dopant is likely the center of the oxygen vacancy cluster. A close inspection of the Bader charges, PDOS and spin density plots of the most stable $Fe@Ce_1$:VO_1 (111) system shows that the formation of an O vacancy leads to the reduction of two Ce^{4+} atoms that are formally Ce^{3+} (see Fig. SI.12).

To define the relative stability of the Fe-doped systems containing different types and or number of atoms depending on pressure and temperature, we have employed the formalism of ab initio thermodynamics as detailed described in the Experimental Section.

Fig. 8 shows a plot of the Gibbs energies ΔG_{ads} (T, p) of the system discussed above as a function of the O chemical potential including a conversion to oxygen partial pressures at several relevant temperatures. It is possible to identify three thermodynamically stable phases. The first phase, which holds for values of $\mu_o > -0.7$ eV, corresponds to the system where a Fe atom substitutes a surface Ce ion, $Fe@Ce_1$ (red line). Under O-rich conditions this structure becomes the thermodynamically most stable one. The second most stable structure is the one obtained by removing a surface O atom from the $Fe@Ce_1$ system (green line). This structure becomes thermodynamically stable in the range $-1.05 < \mu_o < -0.7$ eV (purple line). Finally, for $\mu_o < -1.05$ the $Fe@Ce_1$ system in the presence of two surface O vacancies becomes thermodynamically stable. These findings are in line with the experimental data suggesting that in the presence of Fe atoms substituting Ce ions the formation of O vacancies is favored. In addition, we predict that subsurface substitutional and interstitial Fe doping are never thermodynamically stable (blue and black lines, respectively).

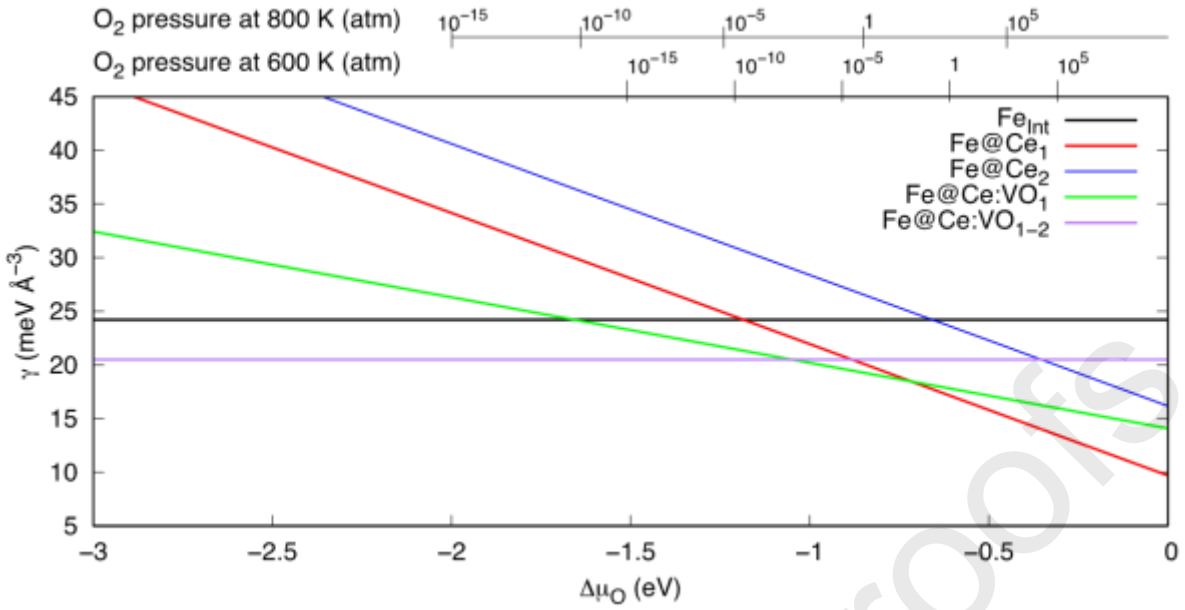

Fig. 8. Gibbs energies ΔG_{ads} (T, p) for substitutional, interstitial Fe atom in CeO_2 (111) and for reduced Fe@Ce_1:VO_1 and Fe@Ce_1:VO_{1-2} (111) as a function of the oxygen chemical potential $\Delta\mu_o$ in eV.

3.3.2. Ibuprofen absorption on the surfaces

The interaction of IBU with stoichiometric (reduced) undoped CeO_2 (111) and the most stable Fe@Ce_1 surfaces was investigated, simulating IBU in its deprotonated form according to the experimental conditions.

Fig. 9 shows the optimized geometries of the most stable configurations of the IBU adsorbed on CeO_2(111), Fe@Ce_1 (111), CeO_2:VO_1(111), and Fe@Ce_1:VO_1(111) (panel a-d, respectively).

IBU interacts with CeO_2(111) through an ionic-like bond between an oxygen atom of its carboxylate group (O^1_{IBU}) and a surface Ce atom of 2.38 Å and an E_{ads} of -0.58 eV (Fig. 9a). In Fe@Ce_1 (111), the ligand binds the surface by a covalent-like bond between O^1_{IBU} and the Fe dopant of 2.12 Å and an E_{ads} of -0.98 (Fig. 9b). In the stoichiometric system, the Fe dopant presence improves the adsorption energy of IBU by 0.4 eV due to i) the greater orbital availability of Fe^{3+} with respect to Ce^{4+} to host electrons and, thus, form new bonds and to ii) the structural distortions generated by the substitutional dopant. In fact, in the presence of Fe, the surface oxygen atom O_1 goes down towards the subsurface oxygen layer allowing a better interaction of the ligand with the Fe@Ce_1 (111) surface.

These energy stabilizations are also reflected in the reduced undoped and Fe-doped systems (Fig. 9c and 9d, respectively). The experiments are performed in aqueous solution and, therefore, water molecules will fill surface O vacancies of the ceria surface leading to a hydroxylated surface. However, if we assume that O vacancies are present on the catalysts, IBU molecules will adsorb on CeO_2@VO_1 (111) and Fe@Ce_1:VO_1 (111) through an ionic and covalent bond of 2.56 and 2.10 Å, respectively, and with E_{ads} of -2.28 and -2.43 eV for the undoped (panel c in Fig.9) and Fe-doped (panel d in Fig.9) reduced systems. Therefore, the hypothetical presence of the surface oxygen vacancy VO_1 improves the ligand E_{ads} of about 1.5 eV with respect to the stoichiometric surfaces as O^2_{IBU} tends to occupy the vacant site stabilizing the IBU adsorption.

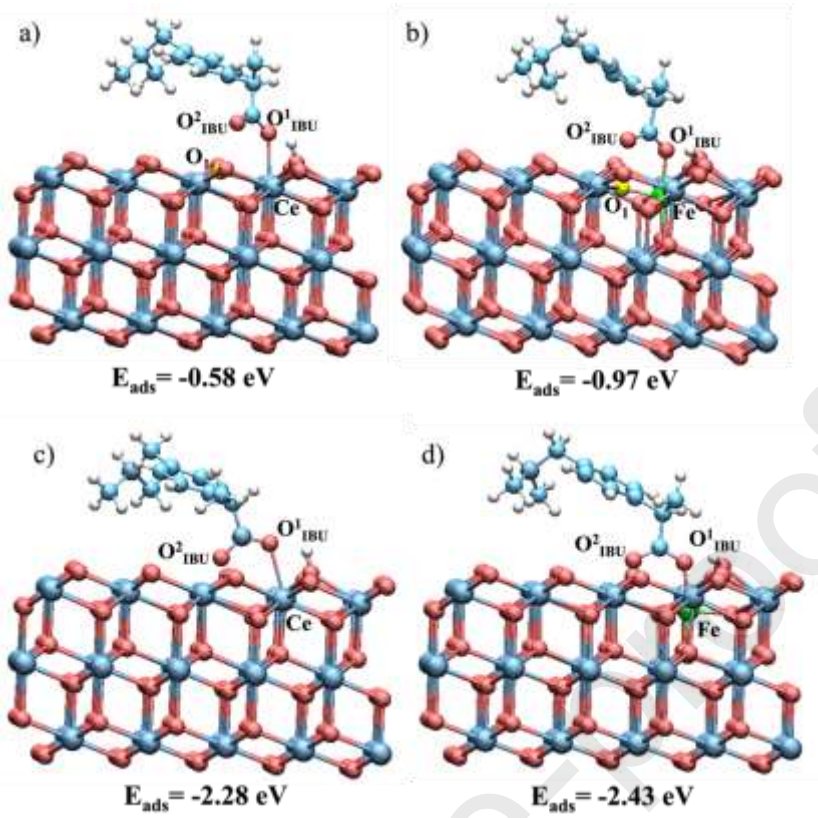

732

733 **Fig. 9**. Optimized structure of a) CeO_2 (111), b) Fe@Ce_1 (111), c) CeO_2@VO_1 (111) and d)
734 Fe@Ce_1:VO_1 (111) with the corresponding E_{ads} (eV). Ce, O and $O^{1\text{-}2}{}_{IBU}$, O_1, C, H and Fe surface
735 atoms are represented in balls and sticks and depicted in blue, red, yellow, cyan, white and green,
736 respectively.

737

738

3.4 *Ibuprofen adsorption and photodegradation activity*

Adsorption and photodegradation tests were conducted to investigate the performance of each synthesized catalyst. An attempt was made to justify the adsorption efficiency with the main properties of the catalysts. Except for the Fe10 sample, we do not observe any significant difference in terms of SSA and pore size. These findings lead us to speculate that the adsorption behaviour of IBU, except for Fe10, should not be determined by textural properties but could reflect differences in surface charge [93]. For this reason, the ζ -potential values at the pH of ibuprofen solution (pH=4.6), extrapolated from the ζ -potential curves (Fig. SI.13), were plotted vs the maximum adsorption capacity (q_t=($C_{IBU,0}$-C_{IBU})/ρ_B), measured in dedicated experiments adopting the following experimental conditions: T=30 °C, $C_{IBU,0}$=12.4 mg L^{-1}, ρ_B = 0.07 g L^{-1}, reaction time of 300 min (Fig. 10a).

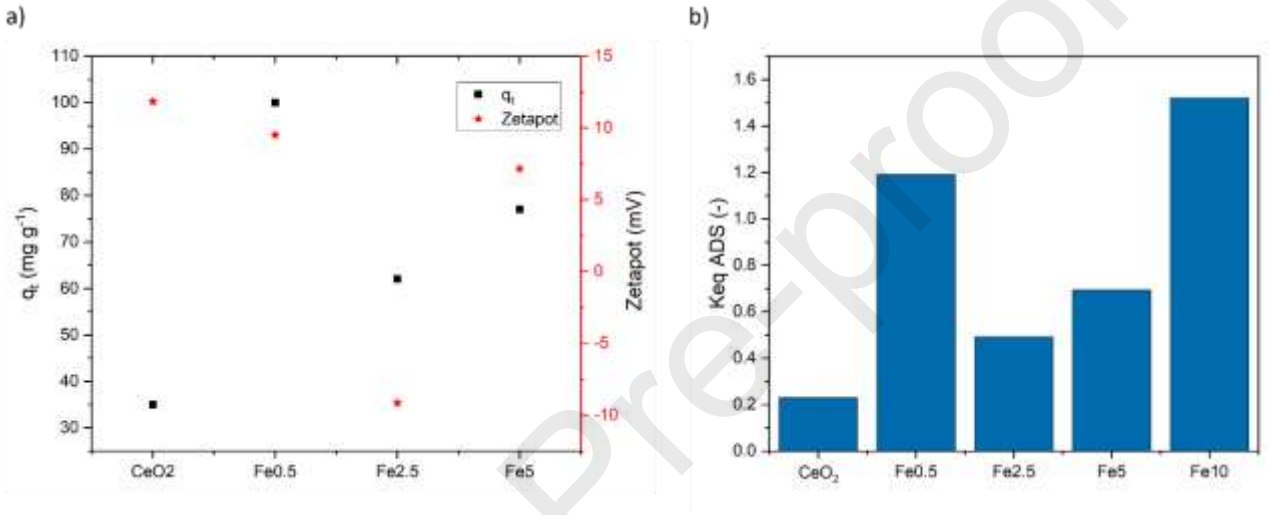

Fig. 10 – a) Potential (ζ) of the pristine and Fe-doped CeO_2 vs the adsorption capacity. b) Trend of the adsorption equilibrium constant. The present experimental conditions were adopted for each experiment: T=30 °C, $C_{IBU,0}$=12.4 mg L^{-1}, ρ_B= 0.07 g L^{-1}, reaction time of 300 min.

From the results shown in Fig. 10a, it is interesting to observe that Fe0.5 and Fe5 samples are positively charged at pH=4.6, namely the pH of the ibuprofen solution, while Fe2.5 is negatively charged. It is worth mentioning that the surface of both ceria and doped ceria is not "naked" but hydroxylated. Thus, being ibuprofen a weak acid (pKa 4.41), in water it is partially dissociated in its anionic form. Therefore, the strongest interactions are expected to be with positively charged materials. Accordingly, the adsorption efficiency passes through a minimum for the Fe2.5 catalyst where the surface is negatively charged, inhibiting the ibuprofen adsorption. The different surface charge may be related to the type of hydroxyls exposed by Fe-CeO_2 surfaces, their distribution and their location with respect to oxygen vacancies [119,120].

The CeO_2 sample shows an opposite trend showing a very low adsorption efficiency even if the surface is positively charged, a finding not explainable by the above-mentioned hypothesis. But it is important to remind that from DFT computations (see Fig. 9), the adsorption energy of ibuprofen improves when it interacts with Fe rather than Ce, clearly leading to a lower adsorption efficiency compared with the samples containing Fe. As previously stated, the Fe10 sample is not included in the trend of doped samples discussion, because of its different properties such as very high surface area and the presence of surface oligomers (*vide supra*) that may promote higher adsorption efficiency. Furthermore, the type of adsorption was further evaluated by FT-IR spectroscopy. The

772 spectra obtained from the Fe2.5 sample and from the same sample after contact with a saturated
773 ibuprofen solution are shown in Fig. SI.14. The spectra show a broad band between 3750 and 3000
774 cm^{-1} due to O-H stretching vibration of surface hydroxyl groups and undissociated water
775 characterized by its bending mode at 1630 cm^{-1} [121,122]. Bands at around 1364 and 1529 cm^{-1} can
776 be attributed to carbonate species, whose presence results from interactions of CeO_2 with atmospheric
777 carbon dioxide [123]. Metal-oxygen vibration are generally observed at low wavenumbers, below
778 800 cm^{-1}. The absence of new chemical bonds in the post-saturation sample, inferred from the
779 absence of new peaks in the saturated Fe2.5 catalyst, suggests a physisorption mechanism.

780 To measure the relative influence of adsorption and photodegradation contribution, the results were
781 interpreted with a simplified kinetic model. The model was written taking into consideration a
782 constant volume ideal batch reactor, where at the beginning of the reaction the ibuprofen solution is
783 loaded to the vessel and the reaction is considered to occur in isothermal conditions. The rate
784 expressions were developed, considering that ibuprofen (IBU) is adsorbed on the surface of the
785 photocatalysts (*) leading to an adsorbed specie (IBU*), as in Eq. 2.

786 $$IBU + * \leftrightarrow IBU^* \quad (2)$$

787 The reversible rate expression reported in Eq. 3 was adopted to describe the adsorption rate.

788 $$r_{ADS} = k_{ADS} \cdot \left(c_{IBU} - \frac{1}{K_{eqADS}} \cdot c_{IBU^*} \right) \quad (3)$$

789 The mentioned rate expression was included in the mass balance equation valid for a batch system,
790 see Eq. 4.

791 $$\frac{dc_{IBU}}{dt} = -r_{ADS} \cdot \rho_B \quad (4)$$

792 The ordinary differential equation was solved in MATLAB R2023a environment, using *ode*45
793 function, and the related adsorption kinetic and equilibrium constants were obtained by parameter
794 estimation activity on the adsorption kinetic experiments. In detail, the objective function, defined as
795 the square root of the squares of the residuals, was minimized using *lsqnonlin* algorithm. The results
796 of the parameter estimation activities are reported in Figs 10b and Table 4.

797 As shown in Fig. 10b, the adsorption equilibrium constants follow the same trend as the adsorption
798 capacity (q_t), being both quantities related to each other whose trend was previously explained via ζ
799 -potential curves. .

800 As adsorption is a physical phenomenon, its velocity depends on the effective diffusivity of ibuprofen
801 molecules in the catalyst pores, thus the lumped kinetic constants reported in Table 4 are dependent
802 on both the porosity and tortuosity of the catalysts. Being the pore volumes of each material very
803 similar (see Table 3), the expected kinetic constants shall fall in the same range, as obtained by
804 parameter estimation and reported in Table 4.

805

806 **Table 4** – Adsorption rate, adsorption equilibrium and degradation rate constants values. The
807 experimental conditions were adopted for each experiment: T=30°C, $C_{IBU,0}$=12.4mg L^{-1}, ρ_B = 0.07 g
808 L^{-1}, reaction time of 300 min.

Sample	k_{ADS} (L g^{-1} min^{-1})	K_{eqADS} (-)	k_{DEG} (L g^{-1} min^{-1})
CeO_2	0.09 ±0.02	0.23 ±0.01	0.03 ±0.01
Fe0.5	0.25 ± 0.01	1.19 ±0.02	0.03 ±0.01
Fe2.5	0.16 ±0.02	0.49 ±0.02	0.11 ±0.01
Fe5	0.23 ±0.02	0.69 ±0.02	0.04 ±0.01
Fe10	0.37 ±0.02	1.52 ±0.03	0.0010± 0.0003

The photodegradation experiments were conducted either in the presence of UV or visible irradiation. The main results are reported in Fig. 11, where it is evident that UV irradiation is slightly more efficient than visible irradiation for all the catalysts. The band gap value of pure ceria settles at the value of 3 eV (see Table 3), which allows the material to mainly exploit the absorption of UV light. The presence of iron in the ceria lattice induces a shift in the onset of absorption in the studied samples. For this reason, the doped samples can be more active under visible irradiation. However, performance between UV and visible irradiation is a delicate balance of several factors, including band gap, surface defects and intra-band gap defect states (that can also act as recombination centres). The performance of the catalysts under visible irradiation is indeed promising for a scale-up process, considering the low lamp power and the used dosage of the catalysts.

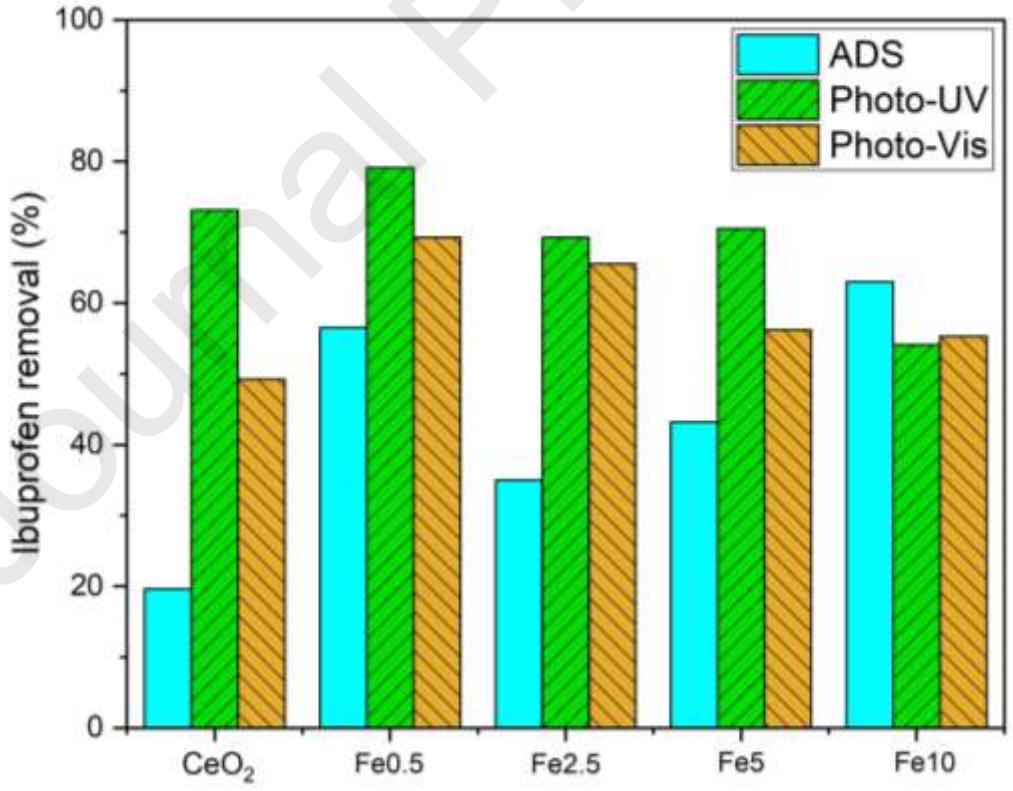

Fig. 11 –Trend of the ibuprofen removal percentage per each catalyst, under either dark or UV or VIS irradiation. The present experimental conditions were adopted for each experiment: T=30°C, $C_{IBU,0}$=12.4 mg L^{-1}, ρ_B=0.07 g L^{-1}, reaction time of 300 min.

Qualitatively, the best catalyst in terms of the overall removal of ibuprofen under visible irradiation is Fe0.5. Nevertheless, it is worth to be mentioned that during the photodegradation experiment, both adsorption and chemical reactions occur. For this reason, we have modified the aforementioned simplified mode, including a degradation step, described by the following rate expression.

$$r_{DEG} = k_{DEG} \cdot c_{\mathrm{IBU}^*} \tag{5}$$

It must be pointed out, that we are implicitly assuming that photodegradation occurs in series to the adsorption process, while it could occur also in parallel. This simplification can be considered reasonable as we are interested in retrieving the order of magnitude of the kinetic constants to compare the activity of each catalyst. Further, the ibuprofen photolysis in the absence of the catalyst was neglected as proved experimentally [113].

Thus, the mass balance equation needs to be further modified, supposing that IBU* undergoes photodegradation, Eq. 6.

$$\frac{dc_{IBU^*}}{dt} = \left(+r_{ADS} - r_{DEG}\right)\rho_B \tag{6}$$

In detail, Fig. 12a shows an example of data fit for the Fe2.5 catalyst: as revealed, a good fit was obtained both for adsorption and photodegradation experiments under visible irradiation. The results of the parameter estimation activities for all catalysts are reported in Table 4 and Fig. 12b.

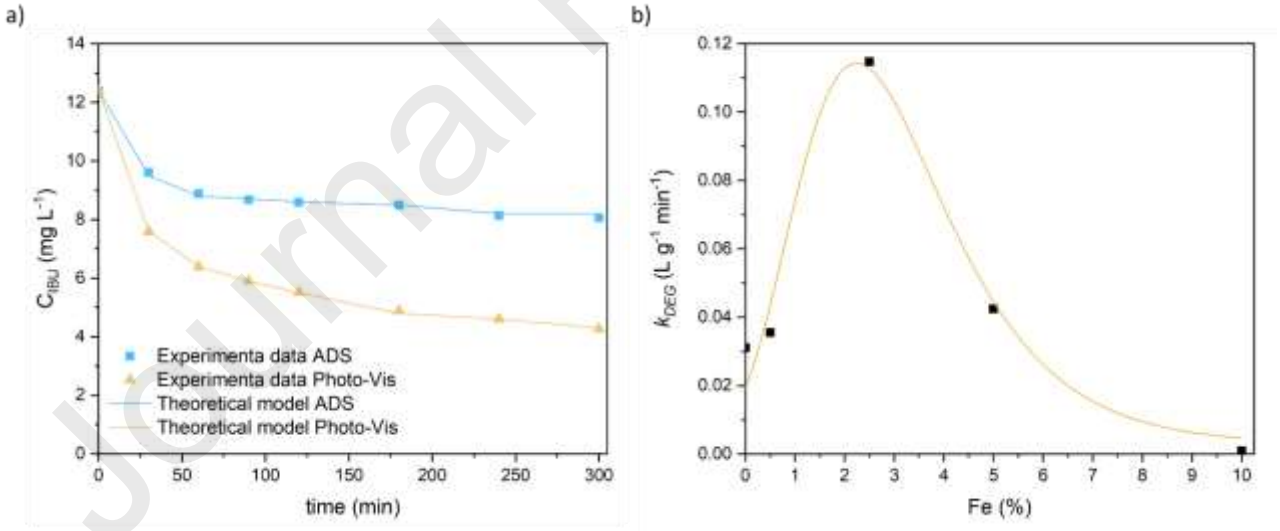

Fig. 12. a) Example of data fit on the kinetic data measured using the Fe2.5 catalyst for both dark and photodegradation experiments under visible irradiation (T=30°C, $C_{\mathrm{IBU},0}$= 12.4 mg L^{-1}, ρ_B= 0.07 g L^{-1}). Symbols represent the experimental data and lines the calculated profiles. b) Plot of the degradation constant as a function of Fe loading.

Fig. 12b clearly illustrates that Fe2.5 is the best performing photocatalyst as it shows the highest degradation constant.

Raman and XPS findings revealed (*vide supra*) that Fe2.5 has the highest content of Ce^{3+} and defects-related oxygen vacancies. Raman results also suggested the highest charge delocalization for Fe2.5 (Fig. 4).

As extensively presented in the literature, the presence of oxygen vacancies can lead to increased photo-oxidation performance as they constitute trapping centres for photogenerated electrons, effectively limiting the rate of electron-hole recombination [124,125].

Finally, by comparing the band gap values with the degradation kinetic constant, it is possible to see that the activity passes through a maximum, as classically reported in the literature [126], thus it is possible to define an optimal band gap value of 2.79 eV (see Table 3).

For the mentioned reasons, it is interesting to further investigate the performance of Fe2.5 in terms of stability. Thus, reuse experiments were conducted under visible light irradiation. As reported in Fig. 13, the activity of Fe2.5 did not change after four cycles of photodegradation tests, demonstrating good stability, thus a potential use in continuous apparatus, allowing the scale-up of the process from batch to continuous operation.

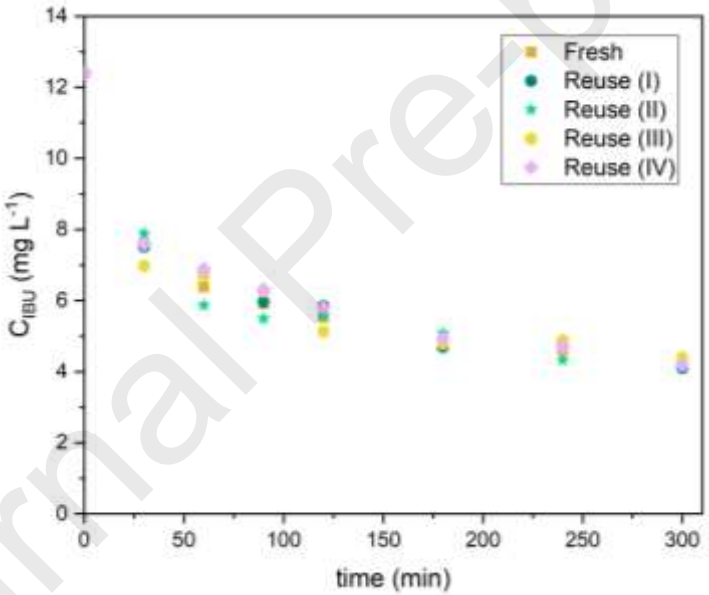

Fig. 13 – Reuse of the photocatalyst Fe2.5 in four photodegradation tests. The present experimental conditions were adopted for each experiment: T = 30°C, $C_{IBU,0}$= 12.4 mg L^{-1}, ρ_B= 0.07 g L^{-1}, reaction time of 300 min.

To further ascertain the stability of the catalyst, some relevant characterizations were conducted on the Fe2.5 sample after the reaction. The obtained results clearly showed no substantial changes in the nanocatalyst properties after the catalytic test. Indeed, the XRD diffraction pattern of the Fe2.5_post reaction (Fig SI.15a) shows the occurrence of the fluorite phase without any significant distortion of the structure.

Thermogravimetric analysis (Fig. SI.15b) analysis reports only a small variation on the region of chemisorbed water compared with the pristine catalyst, indicating that no organic by-products were adsorbed on the catalyst surface.

In accordance with XRD analysis, electron diffraction (see figure Fig. SI.15c) confirms that the cubic fluorite structure of the catalyst is retained after the catalytic tests and that no secondary crystalline phases are formed. The presence of Fe in the nanostructures is recognized by EDX analysis, with comparable EDX spectra (Fig. SI.15d) before and after the catalytic reaction. Moreover, based on HR-TEM images (Fig.SI.15e), it is interesting to notice that the catalytic reaction does not induce morphological or structural changes on the nanoparticles, which also preserve their characteristic size of approximately 5 nm.

Finally, XPS analysis performed on the sample post-catalysis shows first no contamination. Ce3d spectra obtained before and after photocatalysis are quite similar (Fig. SI.16a). A minor change of the v component (at 882.6 eV) can be seen, meaning that the Ce^{4+} contribution may have increased slightly. However, that variation is so small that it hardly affects its 3d3/2 counterpart. Consequently, in accordance with the other analyses, the XPS study confirms that the photocatalytic tests did not induce significant changes in the photocatalyst.

3.4 Identification of degradation by-products

A further objective of this work was the identification of possible degradation products.

The samples collected during the kinetic experiments were analysed via UV-Vis spectrophotometry and allowed the identification of an absorbance peak characteristic of an unknown chemical compound, at the wavelength λ=260 nm. Fig. 14 shows an example of the absorbance spectrum obtained at two different times, collected during a kinetic run conducted imposing the following reaction conditions: catalyst Fe2.5, T=30°C, $C_{IBU,0}$=12.4mg/L, ρ_B=0.07 g/L. In particular, the T0 sample was collected at time=0, while T1 at time = 30 min of reaction time.

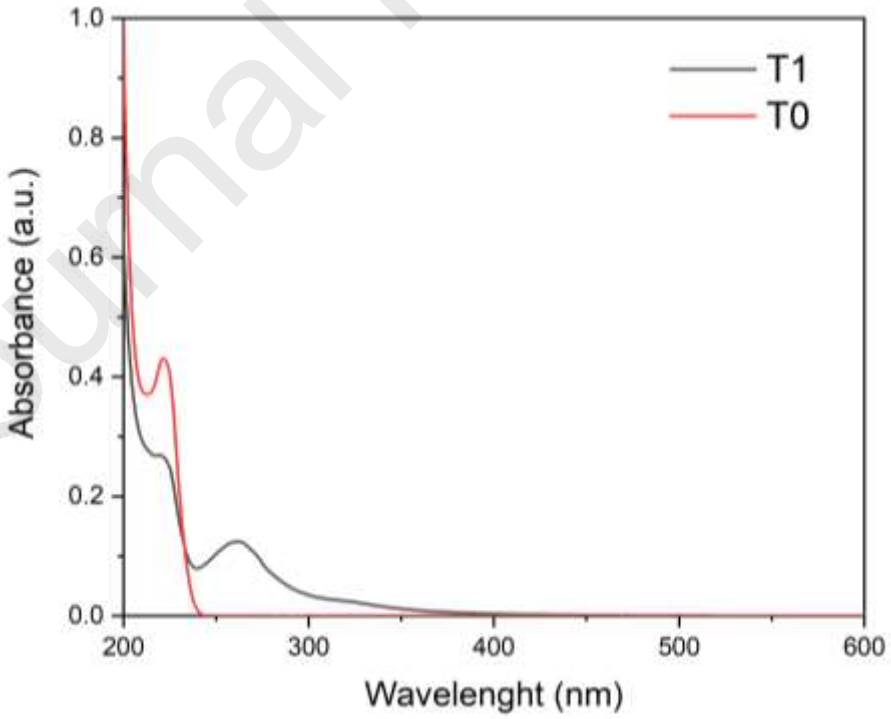

Fig. 14: Comparison between absorbance spectra of samples T0 (sample collected at time = 0) and T1 (sample collected at time = 30 min), collected during a kinetic run conducted imposing the following reaction conditions: catalyst Fe 2.5, T=30°C, $C_{IBU,0}$=12.4mg L^{-1}, ρ_B=0.07 g L^{-1}.

As Fig. 14 reveals, the peak at λ=260 nm is not present when analysing ibuprofen in water solution (T0). The additional peak was detected in every photodegradation test but with an absorbance variable with the experimental time. In particular, the absorbance increases as the reaction proceeds, simultaneously with the decrease of the absorbance measured at λ=220 nm.

Thus, it is important to carry out a more sophisticated analysis to understand the nature of the chemical compounds present during the photodegradation tests. The identification of the by-product generated by the reaction was conducted by performing an adsorption test and subsequent photodegradation. The samples were analysed using a UV-Vis spectrophotometer to monitor the absorbance peaks for ibuprofen and the by-products identified, further identified by LC-MS analysis.

The results obtained from the spectrophotometer analysis are shown in Fig. 15.

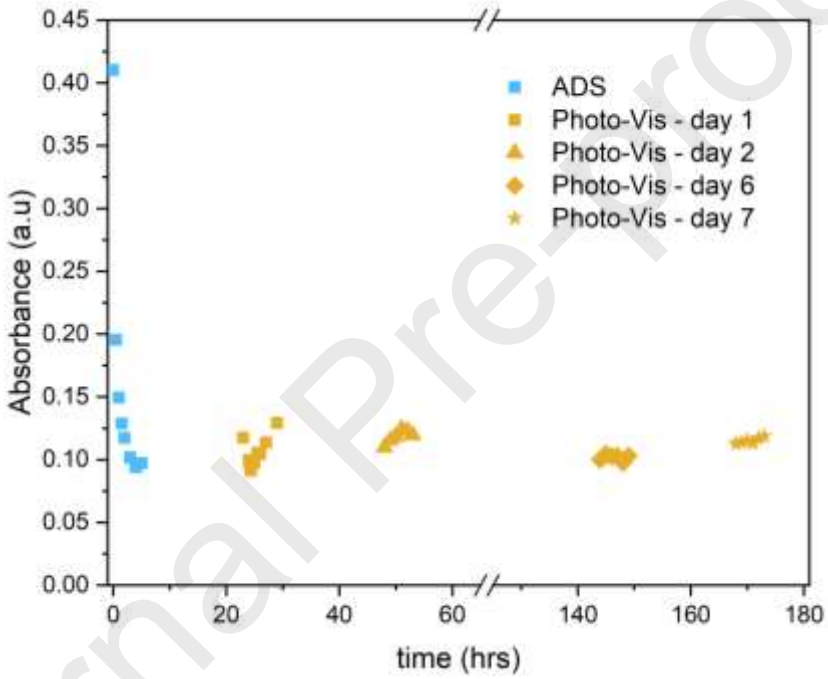

Fig. 15: Results obtained from spectrophotometer analyses. Experimental conditions: catalyst Fe2.5, T = 30°C, $C_{IBU,0}$ = 12.4 mg L^{-1}, ρ_B = 0.07 g L^{-1}.

From the results reported in Fig. 15, it is possible to note that in dark, the absorbance recorded at the wavelength of λ=220 nm decreases, due to a decrease of ibuprofen concentration in the liquid solution due to the related adsorption on the catalyst. Starting from the first day of photodegradation, the absorbance measured at λ=220 nm remains constant for 7 days of reaction. The observed trend could be explained by the formation of by-products, showing an absorption at the same wavelength as ibuprofen.

The identification of neo-formed by-products obtained from the ibuprofen photodegradation was also performed by LC-MS analysis. The MS analysis was preliminarily performed on the standard solution (T0) of ibuprofen to set up the chromatographic conditions and MS parameters. The ion current of the chromatographic peak (3.4 min, Fig. 16 panel A) detected in the mixture at T0 was assigned to the molecular ion ($M+H^+$) of ibuprofen (IBU) at 207.1 m/z in addition to the hydroxylated form

(223.1 m/z) and the sodium adduct species (229.1 m/z) (Fig. 16, exploded panel B). Interestingly, an MS signal at 161.1 m/z was detected in the standard mixture (T0) due to the residue fragmentation occurring within the ESI source causing the loss of formic acid from the starting molecule.

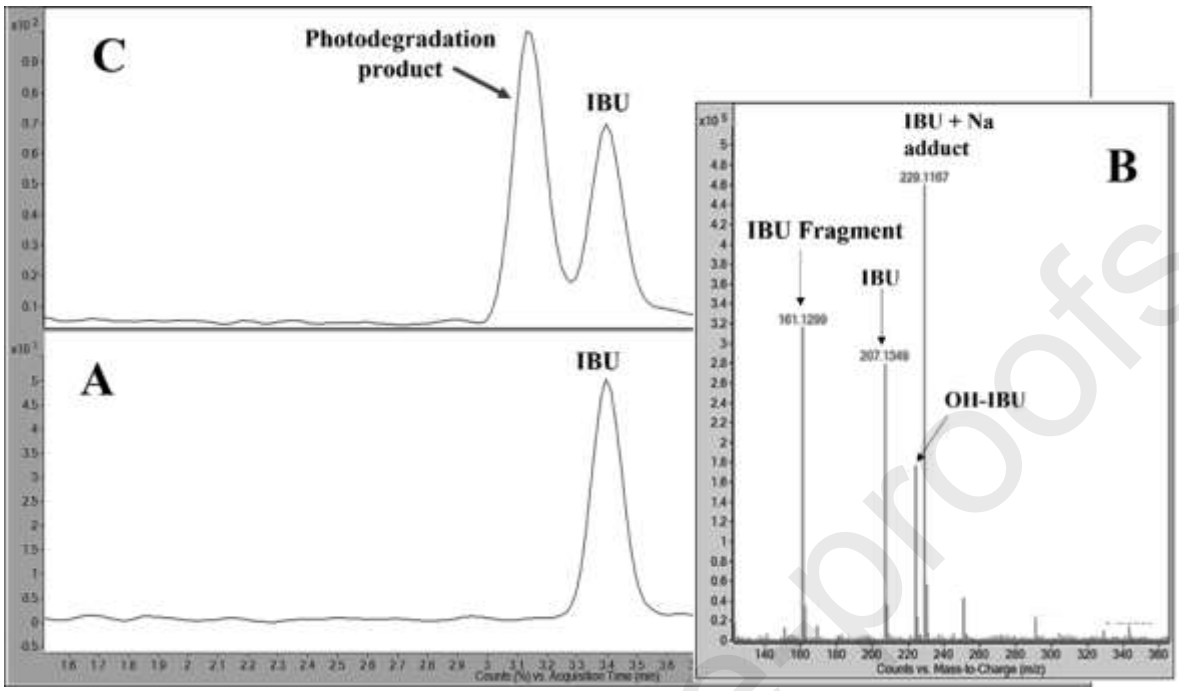

Fig. 16: Total ion current (TIC) chromatogram of the standard mixture (T0) (panel A) and the relative MS spectrum of peak at 3.4 min (panel B). TIC chromatogram of the mixture at the reaction time of 24 h (T10) (panel C).

Then, each aliquot analysed via UV-VIS spectrophotometry was further analysed via LC-TOF, to monitor the formation of the main by-products along the whole photodegradation experiment. The results reported in Fig. 17 demonstrated a marked decrease in ibuprofen after the first 30 min of reaction time (adsorption phase) followed by small variations of the peak area up to T10, Fig. 16 panel C, (roughly 24 h of reaction) till reaching a constant value of roughly the 5% of the initial value (T0 sample) (Fig. 17).

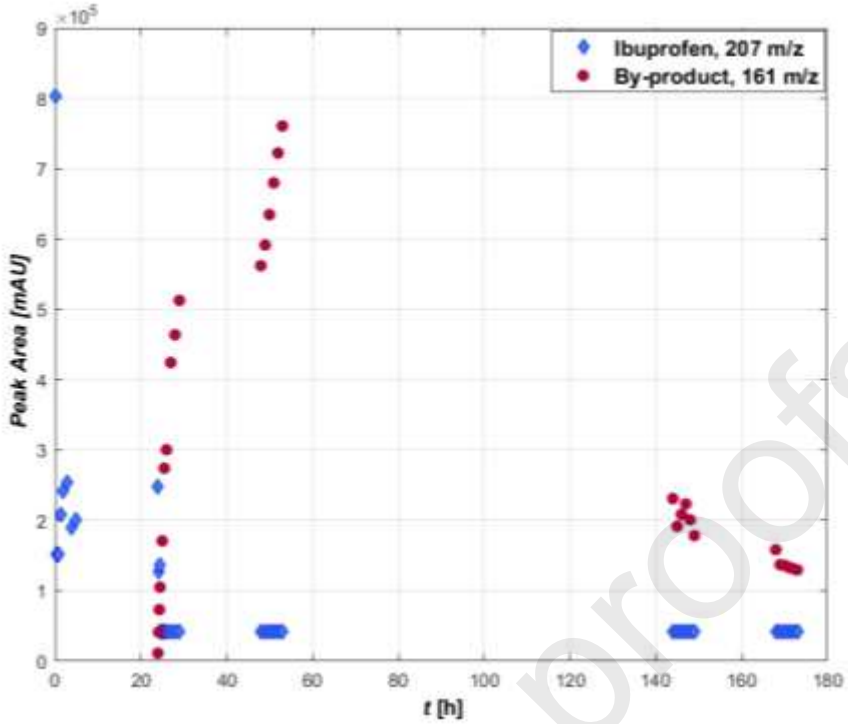

Fig. 17: Monitoring of kinetics of ibuprofen degradation and formation of by-products by mass spectrometry analysis.

The occurrence of neo-formed by-product started to appear at T8, corresponding to the start of the photodegradation step, displaying a chromatographic peak at a retention time shift of 0.3 min (3.1 min) from the intact ibuprofen. The identification of by-product at 161 m/z assigned to the 1-ethenyl-4-(2-methylpropyl)benzene ($C_{12}H_{16}$) was confirmed by GC-MS analysis where the fragments originated from the electron impact (IE) source were compared to the NIST database (Fig. SI.17).

Furthermore, a significant increase of by-product was observed up T23 (roughly after 2 days) where it reached the highest concentration. Then, after the second day, a drastic reduction of the product was recorded.

The presence of the mentioned by-product was already reported in the literature as possible intermediate in a more complex mechanism involving several degradation species In particular, Rao et al., [127], reported that 1-ethenyl-4-(2-methylpropyl)benzene is produced by the dehydration and decomposition of two intermediates as described in Scheme 2. In the present work, the mentioned two intermediates were not detected, probably because the related reactions of formation and disappearance are relatively fast in the presence of Fe2.5 catalyst.

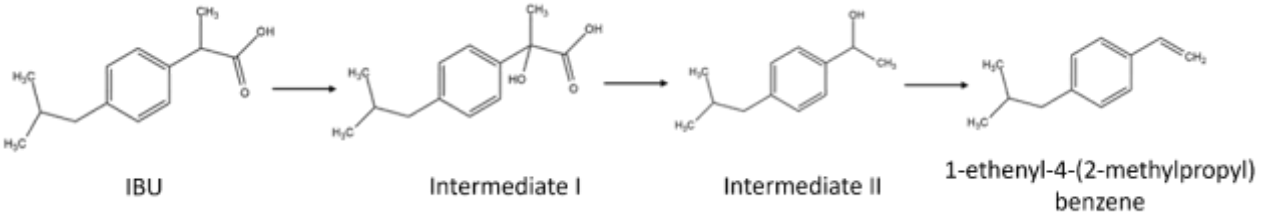

975

976 **Scheme 2:** Possible degradation pathway of IBU with formation of by-product detected in the present
977 study.

978

979

980

Conclusions

Meticulous synthesis strategies for the preparation of robust and efficient photocatalysts are at the forefront of rapidly evolving fields, such as the removal of emerging contaminants in visible light-activated photocatalytic processes.

To avoid a trial and error approach we have selected a reliable and valuable bottom-up approach, the reverse micelle method, that allows to closely control the crystallographic and electronic properties of the ceria nanostructured photocatalysts. With controlled precipitation within the micelle nano-reactors, undoped and iron-substituted (0.50-10 mol %) ceria nanoparticles consisting of single crystals were successfully prepared. The sample with the highest iron content is the only one that shows the presence of oligomeric species on the surface while the other samples show an effective inclusion of substitutional iron in the ceria lattice.

The effect of the different iron content in the various samples revealed the role of iron heteroatoms in the delicate balance between adsorption and relative photodegradation of ibuprofen. Light was shed on the relationship between composition-structure and activity through numerous catalytic experiments, conducted both in the dark and under UV or visible irradiation. The results were supported by a combination of advanced characterisation techniques and DFT calculations, showing that the doping of the CeO_2(111) surface with a substitutional Fe atom i) causes a decrease in the band gap of the system, improving the catalytic performance of the catalyst, ii) favours the formation of vacant sites (VOx) when the oxygen atoms are directly coordinated with the dopant or very close to it, iii) favours the IBU adsorption both in the stoichiometric and reduced model. Despite the presence of iron and vacancies being beneficial for ibuprofen adsorption, experimentally we find a non-linear trend of the adsorption capacity with the iron content. The latter was explained by measuring the z-potential of each sample, finding that adsorption is more efficient when the catalyst surface is positively charged. The combination of this effect and the non-linear trend of ibuprofen adsorption with Fe content leads to the identification of an optimal composition of the photocatalyst, namely 2.5 mol% Fe doped CeO_2. The mentioned material showed good stability along 4 cycles of re-use experiments, demonstrating to be a promising material for a future application in flow.

Finally, GC-MS and HPLC-MS analyses were conducted on the samples collected in a dedicated experiment conducted with Fe2.5 catalyst under visible irradiation, allowing the identification of 1-ethenyl-4-(2-methylpropyl)benzene as the main by-product.

1013 ***List of abbreviations***

IBU	*Ibuprofen*
(*)	*Free site*
(IBU)	*Ibuprofen*
(IBU)*	*Ibuprofen adsorbed into the solid*
AOPs	*Advanced oxidation processes*
NSAIDs	*Non-steroidal anti-inflammatory drugs*

1014

1015 ***List of symbols***

$C_{IBU,0}$	*ibuprofen initial concentration*	*(mg L^{-1})*
C_{IBU}	*concentration of ibuprofen at t time*	*(mg L^{-1})*
C_{IBU*}	*concentration of adsorbed ibuprofen*	*(mg L^{-1})*
k_{ADS}	*adsorption kinetic constant*	*(L (g min)$^{-1}$)*
k_{DEG}	*desorption kinetic constant*	*(L (g min)$^{-1}$)*
K_{eqADS}	*adsorption constant*	*(-)*
qt	*adsorbed amount*	*(mg g^{-1})*
r_{ADS}	*adsorption rate*	*(mg g^{-1} min^{-1})*
r_{DEG}	*desorption rate*	*(mg g^{-1} min^{-1})*
t	*time*	*(min)*
T	*temperature*	*(°C)*

Greek symbol

ρ_B *sorbent bulk density* *(g* L^{-1}*)*

Acknowledgments

Miss Sonia Romano is cordially acknowledged for the experimental and numerical support given for the realization of the present study.

Reference

1. Shah, A.H.; Rather, M.A.; Shah, A.H.; Rather, M.A. Advances in Nano Research. *Adv Nano Res* **2021**, *10*, 397, doi:10.12989/ANR.2021.10.4.397.

2. Nath Bhadra, B.; Ahmed, I.; Kim, S.; Jhung, S.H. Adsorptive Removal of Ibuprofen and Diclofenac from Water Using Metal-Organic Framework-Derived Porous Carbon., doi:10.1016/j.cej.2016.12.127.

3. Madikizela, L.M.; Chimuka, L. Simultaneous Determination of Naproxen, Ibuprofen and Diclofenac in Wastewater Using Solid-Phase Extraction with High Performance Liquid Chromatography. *Water SA* **2017**, *43*, 264, doi:10.4314/wsa.v43i2.10.

4. Oba, S.N.; Ighalo, J.O.; Aniagor, C.O.; Igwegbe, A. Removal of Ibuprofen from Aqueous Media by Adsorption: A Comprehensive Review. *Science of the Total Environment* **2021**, *780*, 146608, doi:10.1016/j.scitotenv.2021.146608.

5. Ohtani, B. Photocatalysis A to Z-What We Know and What We Do Not Know in a Scientific Sense. *Journal of Photochemistry and Photobiology C: Photochemistry Reviews* **2010**, *11*, 157–178, doi:10.1016/j.jphotochemrev.2011.02.001.

6. Nan Chong, M.; Jin, B.; Chow, C.W.; Saint, C. Recent Developments in Photocatalytic Water Treatment Technology: A Review. *Water Res* **2010**, *44*, 2997–3027, doi:10.1016/j.watres.2010.02.039.

7. Melchionna, M.; Fornasiero, P. Updates on the Roadmap for Photocatalysis. **2020**, doi:10.1021/acscatal.0c01204.

8. Mancuso, A.; Morante, N.; De Carluccio, M.; Sacco, O.; Rizzo, L.; Fontana, M.; Esposito, S.; Vaiano, V.; Sannino, D. Solar Driven Photocatalysis Using Iron and Chromium Doped TiO2 Coupled to Moving Bed Biofilm Process for Olive Mill Wastewater Treatment. *Chemical Engineering Journal* **2022**, *450*, 138107, doi:10.1016/j.cej.2022.138107.

9. Lou, L.; Wang, J.; Joon Lee, Y.; Ramkumar, S.S.; Lou, L.; Ramkumar, S.S.; Wang, J.; Lee, Y.J. Visible Light Photocatalytic Functional TiO2/PVDF Nanofibers for Dye Pollutant Degradation. *Particle & Particle Systems Characterization* **2019**, *36*, 1900091, doi:10.1002/PPSC.201900091.

10. Iervolino, G.; Zammit, I.; Vaiano, V.; Rizzo, L. Limitations and Prospects for Wastewater Treatment by UV and Visible-Light-Active Heterogeneous Photocatalysis: A Critical Review. *Top Curr Chem* **2020**, *378*, 7, doi:10.1007/s41061-019-0272-1.

11. Tammaro, O.; Morante, N.; Marocco, A.; Fontana, M.; Castellino, M.; Barrera, G.; Allia, P.; Tiberto, P.; Arletti, R.; Fantini, R.; et al. The Beneficial Role of Nano-Sized Fe3O4 Entrapped in Ultra-Stable Y Zeolite for the Complete Mineralization of Phenol by Heterogeneous Photo-Fenton under Solar Light. *Chemosphere* **2023**, *345*, 140400, doi:10.1016/j.chemosphere.2023.140400.

12. El-Sheikh, S.M.; Khedr, T.M.; Hakki, A.; Ismail, A.A.; Badawy, W.A.; Bahnemann, D.W. Visible Light Activated Carbon and Nitrogen Co-Doped Mesoporous TiO2 as Efficient Photocatalyst for Degradation of Ibuprofen. *Sep Purif Technol* **2017**, *173*, 258–268, doi:10.1016/J.SEPPUR.2016.09.034.

13. Liu, N.; Wang, J.; Wu, J.; Li, Z.; Huang, W.; Zheng, Y.; Lei, J.; Zhang, X.; Tang, L. Magnetic Fe 3 O 4 @MIL-53(Fe) Nanocomposites Derived from MIL-53(Fe) for the Photocatalytic Degradation of Ibuprofen under Visible Light Irradiation. **2020**, doi:10.1016/j.materresbull.2020.111000.

14. Sarafraz, M.; Amini, M.M.; Adiban, M.; Eslami, A. Facile Synthesis of Mesoporous Black N–TiO2 Photocatalyst for Efficient Charge Separation and the Visible-Driven Photocatalytic Mechanism of Ibuprofen Degradation. *Mater Sci Semicond Process* **2020**, *120*, 105258, doi:10.1016/J.MSSP.2020.105258.

15. Liu, N.; Fei, F.; Dai, W.; Lei, J.; Bi, F.; Wang, B.; Quan, G.; Zhang, X.; Tang, L. Visible-Light-Assisted Persulfate Activation by SnS2/MIL-88B(Fe) Z-Scheme Heterojunction for Enhanced Degradation of Ibuprofen. *J Colloid Interface Sci* **2022**, *625*, 965–977, doi:10.1016/J.JCIS.2022.06.099.

16. Liu, N.; Wu, J.; Fei, F.; Lei, J.; Shi, W.; Quan, G.; Zeng, S.; Zhang, X.; Tang, L. Ibuprofen Degradation by a Synergism of Facet-Controlled MIL-88B(Fe) and Persulfate under Simulated Visible Light., doi:10.1016/j.jcis.2021.12.142.

17. Chaker, H.; Fourmentin, S.; Chérif-Aouali, L. Efficient Photocatalytic Degradation of Ibuprofen under Visible Light Irradiation Using Silver and Cerium Co-Doped Mesoporous TiO $_2$. *ChemistrySelect* **2020**, *5*, 11787–11796, doi:10.1002/slct.202002730.

18. Montini, T.; Melchionna, M.; Monai, M.; Fornasiero, P. Fundamentals and Catalytic Applications of CeO 2-Based Materials. **2016**, doi:10.1021/acs.chemrev.5b00603.

19. Mansingh, S.; Padhi, D.K.; Parida, K.M. Enhanced Photocatalytic Activity of Nanostructured Fe Doped CeO2 for Hydrogen Production under Visible Light Irradiation. *Int J Hydrogen Energy* **2016**, *41*, 14133–14146, doi:10.1016/j.ijhydene.2016.05.191.

20. Corma, A.; Atienzar, P.; García, H.; Chane-Ching, J.-Y. Hierarchically Mesostructured Doped CeO2 with Potential for Solar-Cell Use. *Nat Mater* **2004**, *3*, 394–397, doi:10.1038/nmat1129.

21. Kusmierek, E. A CeO2 Semiconductor as a Photocatalytic and Photoelectrocatalytic Material for the Remediation of Pollutants in Industrial Wastewater: A Review. *Catalysts* **2020**, *10*, 1435, doi:10.3390/catal10121435.

22. Ma, R.; Zhang, S.; Wen, T.; Gu, P.; Li, L.; Zhao, G.; Niu, F.; Huang, Q.; Tang, Z.; Wang, X. A Critical Review on Visible-Light-Response CeO2-Based Photocatalysts with Enhanced Photooxidation of Organic Pollutants. *Catal Today* **2019**, *335*, 20–30, doi:10.1016/J.CATTOD.2018.11.016.

23. Atran, A.A.; Hamdy, M.S. Improving the Photocatalytic Performance of Porous Ceria under Visible Light Illumination via Mn Incorporation. *Catalysts* **2023**, *13*, 523, doi:10.3390/catal13030523.

24. Tsoncheva, T.; Rosmini, C.; Dimitrov, M.; Issa, G.; Henych, J.; Němečková, Z.; Kovacheva, D.; Velinov, N.; Atanasova, G.; Spassova, I. Formation of Catalytic Active Sites in Hydrothermally Obtained Binary Ceria-Iron Oxides: Composition and Preparation Effects. *ACS Appl Mater Interfaces* **2021**, *13*, 1838–1852, doi:10.1021/ACSAMI.0C16326/ASSET/IMAGES/LARGE/AM0C16326_0011.JPEG.

25. Liu, B.; Yan, Z.; Xu, T.; Li, C.; Gao, R.; Hao, H.; Bai, J. Co-Construction of Oxygen Vacancies and Heterojunctions on CeO2 via One-Step Fe Doping for Enhanced Photocatalytic Activity in Suzuki Reaction. *Chemical Engineering Journal* **2022**, *442*, 136226, doi:10.1016/J.CEJ.2022.136226.

26. *Cerium Oxide (CeO_2): Synthesis, Properties and Applications*; Elsevier, 2020; ISBN 9780128156612.

27. Younis, A.; Chu, D.; Kaneti, Y.V.; Li, S. Tuning the Surface Oxygen Concentration of {111} Surrounded Ceria Nanocrystals for Enhanced Photocatalytic Activities. *Nanoscale* **2015**, *8*, 378–387, doi:10.1039/C5NR06588G.

28. Choudhury, B.; Chetri, P.; Choudhury, A. Oxygen Defects and Formation of Ce3+ Affecting the Photocatalytic Performance of CeO2 Nanoparticles. *RSC Adv* **2013**, *4*, 4663–4671, doi:10.1039/C3RA44603D.

29. Trovarelli, A. Structural and Oxygen Storage/Release Properties of CeO 2-Based Solid Solutions. *Comments on Inorganic Chemistry* **1999**, *20*, 263–284, doi:10.1080/02603599908021446.

30. TROVARELLI, A. Catalytic Properties of Ceria and CeO_2 -Containing Materials. *Catalysis Reviews* **1996**, *38*, 439–520, doi:10.1080/01614949608006464.

31. Zhang, F.; Zhao, L.; Chen, H.; He, Y.; Tian, P.; Zeng, X. Synthesis of Mesoporous Fe/h-CeO_2 Hollow Micro-Spheres with Enhanced Visible Light Photocatalytic Activity. *Mater Res Express* **2019**, *6*, 095516, doi:10.1088/2053-1591/ab3015.

32. Cai, W.; Chen, F.; Shen, X.; Chen, L.; Zhang, J. Enhanced Catalytic Degradation of AO7 in the CeO2-H2O2 System with Fe3+ Doping. *Appl Catal B* **2010**, *101*, 160–168, doi:10.1016/J.APCATB.2010.09.031.

33. Channei, D.; Inceesungvorn, B.; Wetchakun, N.; Ukritnukun, S.; Nattestad, A.; Chen, J.; Phanichphant, S. Photocatalytic Degradation of Methyl Orange by CeO2 and Fe–Doped CeO2 Films under Visible Light Irradiation. *Sci Rep* **2014**, *4*, 5757, doi:10.1038/srep05757.

34. Zhao, B.; Shao, Q.; Hao, L.; Zhang, L.; Liu, Z.; Zhang, B.; Ge, S.; Guo, Z. Yeast-Template Synthesized Fe-Doped Cerium Oxide Hollow Microspheres for Visible Photodegradation of Acid Orange 7. *J Colloid Interface Sci* **2018**, *511*, 39–47, doi:10.1016/J.JCIS.2017.09.077.

35. Wang, Y.; Wang, F.; Chen, Y.; Zhang, D.; Li, B.; Kang, S.; Li, X.; Cui, L. Enhanced Photocatalytic Performance of Ordered Mesoporous Fe-Doped CeO2 Catalysts for the Reduction of CO2 with H2O under Simulated Solar Irradiation. *Appl Catal B* **2014**, *147*, 602–609, doi:10.1016/j.apcatb.2013.09.036.

36. Channei, D.; Inceesungvorn, B.; Wetchakun, N.; Phanichphant, S.; Nakaruk, A.; Koshy, P.; Sorrell, C.C. Photocatalytic Activity under Visible Light of Fe-Doped CeO2 Nanoparticles Synthesized by Flame Spray Pyrolysis. *Ceram Int* **2013**, *39*, 3129–3134, doi:10.1016/j.ceramint.2012.09.093.

37. Esposito, S. Introduction. In *Sol-Gel Synthesis Strategies for Tailored Catalytic Materials* ; 2023; pp. 1–12, https://doi.org/10.1007/978-3-031-20723-5_1.

38. Pileni, M.P. Reverse Micelles as Microreactors. *J Phys Chem* **1993**, *97*, 6961–6973, doi:10.1021/j100129a008.

39. Moragues, T.; Arguijo, D.; Beneyton, T.; Modavi, C.; Simutis, K.; Abate, A.R.; Baret, J.-C.; deMello, A.J.; Densmore, D.; Griffiths, A.D. Droplet-Based Microfluidics. *Nature Reviews Methods Primers* **2023**, *3*, 32, doi:10.1038/s43586-023-00212-3.

40. Omidi, M.; Almeida, L.; Tayebi, L. Microfluidic-assisted Fabrication of Reverse Micelle/PLGA Hybrid Microspheres for Sustained Vascular Endothelial Growth Factor Delivery. *Biotechnol Appl Biochem* **2021**, *68*, 616–625, doi:10.1002/bab.1971.

41. Quinlan, F.T.; Kuther, J.; Tremel, W.; Knoll, W.; Risbud, S.; Stroeve, P. Reverse Micelle Synthesis and Characterization of ZnSe Nanoparticles. *Langmuir* **2000**, *16*, 4049–4051, doi:10.1021/la9909291.

42. Morrison, S.A.; Cahill, C.L.; Carpenter, E.E.; Harris, V.G. Production Scaleup of Reverse Micelle Synthesis. *Ind Eng Chem Res* **2006**, *45*, 1217–1220, doi:10.1021/ie050886l.

43. Tammaro, O.; Costagliola di Polidoro, A.; Romano, E.; Netti, P.A.; Torino, E. A Microfluidic Platform to Design Multimodal PEG - Crosslinked Hyaluronic Acid Nanoparticles (PEG-CHANPs) for Diagnostic Applications. *Sci Rep* **2020**, *10*, doi:10.1038/s41598-020-63234-x.

44. Lee, Y.; Lee, J.; Bae, C.J.; Park, J.-G.; Noh, H.-J.; Park, J.-H.; Hyeon, T. Large-Scale Synthesis of Uniform and Crystalline Magnetite Nanoparticles Using Reverse Micelles as Nanoreactors under Reflux Conditions. *Adv Funct Mater* **2005**, *15*, 503–509, doi:10.1002/adfm.200400187.

45. Arsene, M.-L.; Răut, I.; Călin, M.; Jecu, M.-L.; Doni, M.; Gurban, A.-M. Versatility of Reverse Micelles: From Biomimetic Models to Nano (Bio)Sensor Design. *Processes* **2021**, *9*, 345, doi:10.3390/pr9020345.

46. Laguna, O.H.; Centeno, M.A.; Boutonnet, M.; Odriozola, J.A. Fe-Doped Ceria Solids Synthesized by the Microemulsion Method for CO Oxidation Reactions. *Appl Catal B* **2011**, *106*, 621–629, doi:10.1016/j.apcatb.2011.06.025.

47. Pournajaf, R.; Hassanzadeh-Tabrizi, S.A.; Jafari, M. Reverse Microemulsion Synthesis of CeO2 Nanopowder Using Polyoxyethylene(23)Lauryl Ether as a Surfactant. *Ceram Int* **2014**, *40*, 8687–8692, doi:10.1016/j.ceramint.2014.01.086.

48. Tescione, F.; Tammaro, O.; Bifulco, A.; Del Monaco, G.; Esposito, S.; Pansini, M.; Silvestri, B.; Costantini, A. Silica Meets Tannic Acid: Designing Green Nanoplatforms for Environment Preservation. *Molecules* **2022**, *27*, 1944, doi:10.3390/molecules27061944.

49. Addorisio, V.; Pirozzi, D.; Esposito, S.; Sannino, F. Decontamination of Waters Polluted with Simazine by Sorption on Mesoporous Metal Oxides. *J Hazard Mater* **2011**, *196*, 242–247, doi:10.1016/j.jhazmat.2011.09.022.

50. Perdew, J.P.; Burke, K.; Ernzerhof, M. Generalized Gradient Approximation Made Simple. *Phys Rev Lett* **1996**, *77*, 3865–3868, doi:10.1103/PhysRevLett.77.3865.

51. Vanderbilt, D. Soft Self-Consistent Pseudopotentials in a Generalized Eigenvalue Formalism. *Phys Rev B* **1990**, *41*, 7892–7895, doi:10.1103/PhysRevB.41.7892.

52. Giannozzi, P.; Andreussi, O.; Brumme, T.; Bunau, O.; Buongiorno Nardelli, M.; Calandra, M.; Car, R.; Cavazzoni, C.; Ceresoli, D.; Cococcioni, M.; et al. Advanced Capabilities for Materials Modelling with Quantum ESPRESSO. *Journal of Physics: Condensed Matter* **2017**, *29*, 465901, doi:10.1088/1361-648X/aa8f79.

53. Cococcioni, M.; de Gironcoli, S. Linear Response Approach to the Calculation of the Effective Interaction Parameters in the <math Display="inline"> <mrow> <mi>LDA</Mi> <mo>+</Mo> <mi Mathvariant="normal">U</Mi> </Mrow> </Math> Method. *Phys Rev B* **2005**, *71*, 035105, doi:10.1103/PhysRevB.71.035105.

54. Loschen, C.; Carrasco, J.; Neyman, K.M.; Illas, F. First-Principles <math Display="inline"> <mrow> <mi>LDA</Mi> <mo>+</Mo> <mi Mathvariant="normal">U</Mi> </Mrow> </Math> and <math Display="inline"> <mrow> <mi>GGA</Mi> <mo>+</Mo> <mi Mathvariant="normal">U</Mi> </Mrow> </Math> Study of Cerium Oxides: Dependence on the Effective U Parameter. *Phys Rev B* **2007**, *75*, 035115, doi:10.1103/PhysRevB.75.035115.

55. Fabris, S.; Vicario, G.; Balducci, G.; de Gironcoli, S.; Baroni, S. Electronic and Atomistic Structures of Clean and Reduced Ceria Surfaces. *J Phys Chem B* **2005**, *109*, 22860–22867, doi:10.1021/jp0511698.

56. Nolan, M.; Grigoleit, S.; Sayle, D.C.; Parker, S.C.; Watson, G.W. Density Functional Theory Studies of the Structure and Electronic Structure of Pure and Defective Low Index Surfaces of Ceria. *Surf Sci* **2005**, *576*, 217–229, doi:10.1016/j.susc.2004.12.016.

57. Nolan, M.; Watson, G.W. The Surface Dependence of CO Adsorption on Ceria. *J Phys Chem B* **2006**, *110*, 16600–16606, doi:10.1021/jp062499a.

58. Da Silva, J.L.F.; Ganduglia-Pirovano, M.V.; Sauer, J.; Bayer, V.; Kresse, G. Hybrid Functionals Applied to Rare-Earth Oxides: The Example of Ceria. *Phys Rev B* **2007**, *75*, 045121, doi:10.1103/PhysRevB.75.045121.

59. Zhang, C.; Michaelides, A.; King, D.A.; Jenkins, S.J. Structure of Gold Atoms on Stoichiometric and Defective Ceria Surfaces. *J Chem Phys* **2008**, *129*, 194708, doi:10.1063/1.3009629.

60. Yue, L.; Zhang, X.-M. Structural Characterization and Photocatalytic Behaviors of Doped CeO2 Nanoparticles. *J Alloys Compd* **2009**, *475*, 702–705, doi:10.1016/j.jallcom.2008.07.096.

61. Ganduglia-Pirovano, M.V.; Da Silva, J.L.F.; Sauer, J. Density-Functional Calculations of the Structure of Near-Surface Oxygen Vacancies and Electron Localization on <math Display="inline"> <msub> <mi>CeO</Mi> <mn>2</Mn> </Msub> <mo Stretchy="false">(</Mo> <mn>111</Mn> <mo Stretchy="false">)</Mo> </Math>. *Phys Rev Lett* **2009**, *102*, 026101, doi:10.1103/PhysRevLett.102.026101.

62. Szabová, L.; Camellone, M.F.; Huang, M.; Matolín, V.; Fabris, S. Thermodynamic, Electronic and Structural Properties of Cu/CeO2 Surfaces and Interfaces from First-Principles DFT+U Calculations. *J Chem Phys* **2010**, *133*, 234705, doi:10.1063/1.3515424.

63. Chen, A.; Yu, X.; Zhou, Y.; Miao, S.; Li, Y.; Kuld, S.; Sehested, J.; Liu, J.; Aoki, T.; Hong, S.; et al. Structure of the Catalytically Active Copper–Ceria Interfacial Perimeter. *Nat Catal* **2019**, *2*, 334–341, doi:10.1038/s41929-019-0226-6.

64. Tran, N.-D.; Farnesi Camellone, M.; Fabris, S. Probing the Reactivity of Pt/Ceria Nanocatalysts toward Methanol Oxidation: From Ionic Single-Atom Sites to Metallic Nanoparticles. *The Journal of Physical Chemistry C* **2018**, *122*, 17917–17927, doi:10.1021/acs.jpcc.8b05735.

65. Dvořák, F.; Szabová, L.; Johánek, V.; Farnesi Camellone, M.; Stetsovych, V.; Vorokhta, M.; Tovt, A.; Skála, T.; Matolínová, I.; Tateyama, Y.; et al. Bulk Hydroxylation and Effective Water Splitting by Highly Reduced Cerium Oxide: The Role of O Vacancy Coordination. *ACS Catal* **2018**, *8*, 4354–4363, doi:10.1021/acscatal.7b04409.

66. Oh, S.; Shin, W.S.; Kim, H.T. Effects of PH, Dissolved Organic Matter, and Salinity on Ibuprofen Sorption on Sediment. *Environmental Science and Pollution Research* **2016**, *23*, 22882–22889, doi:10.1007/s11356-016-7503-6.

67. Ritacco, I.; Imparato, C.; Falivene, L.; Cavallo, L.; Magistrato, A.; Caporaso, L.; Farnesi Camellone, M.; Aronne, A. Spontaneous Production of Ultrastable Reactive Oxygen Species on Titanium Oxide Surfaces Modified with Organic Ligands. *Adv Mater Interfaces* **2021**, *8*, 2100629, doi:10.1002/admi.202100629.

68. Finkelstein-Shapiro, D.; Davidowski, S.K.; Lee, P.B.; Guo, C.; Holland, G.P.; Rajh, T.; Gray, K.A.; Yarger, J.L.; Calatayud, M. Direct Evidence of Chelated Geometry of Catechol on TiO_2 by a Combined Solid-State NMR and DFT Study. *The Journal of Physical Chemistry C* **2016**, *120*, 23625–23630, doi:10.1021/acs.jpcc.6b08041.

69. Liu, L.-M.; Li, S.-C.; Cheng, H.; Diebold, U.; Selloni, A. Growth and Organization of an Organic Molecular Monolayer on TiO_2 : Catechol on Anatase (101). *J Am Chem Soc* **2011**, *133*, 7816–7823, doi:10.1021/ja200001r.

70. Guo, L.; Huang, Y.; Ritacca, A.G.; Wang, K.; Ritacco, I.; Tan, Y.; Qiang, Y.; Al-Zaqri, N.; Shi, W.; Zheng, X. Effect of Indole-2-Carboxylic Acid on the Self-Corrosion and Discharge Activity of Aluminum Alloy Anode in Alkaline Al–Air Battery. *Molecules* **2023**, *28*, 4193, doi:10.3390/molecules28104193.

71. Kaxiras, E.; Bar-Yam, Y.; Joannopoulos, J.D.; Pandey, K.C. *Ab Initio* Theory of Polar Semiconductor Surfaces. I. Methodology and the (*22*) Reconstructions of GaAs(111). *Phys Rev B* **1987**, *35*, 9625–9635, doi:10.1103/PhysRevB.35.9625.

72. Qian, G.-X.; Martin, R.M.; Chadi, D.J. First-Principles Study of the Atomic Reconstructions and Energies of Ga- and As-Stabilized GaAs(100) Surfaces. *Phys Rev B* **1988**, *38*, 7649–7663, doi:10.1103/PhysRevB.38.7649.

73. Reuter, K.; Scheffler, M. Composition, Structure, and Stability of <math Display="inline"> <mrow> <msub> <mrow> <mi Mathvariant="normal">RuO</Mi> </Mrow> <mrow> <mn>2</Mn> </Mrow> </Msub> </Mrow> <mn/> <mo>(</Mo> <mn>110</Mn> <mo>)</Mo> <mn/> </Math> as a Function of Oxygen Pressure. *Phys Rev B* **2001**, *65*, 035406, doi:10.1103/PhysRevB.65.035406.

74. Meyer, B. First-Principles Study of the Polar O-Terminated ZnO Surface in Thermodynamic Equilibrium with Oxygen and Hydrogen. *Phys Rev B* **2004**, *69*, 045416, doi:10.1103/PhysRevB.69.045416.

75. Henkelman, G.; Arnaldsson, A.; Jónsson, H. A Fast and Robust Algorithm for Bader Decomposition of Charge Density. *Comput Mater Sci* **2006**, *36*, 354–360, doi:10.1016/j.commatsci.2005.04.010.

76. Sanville, E.; Kenny, S.D.; Smith, R.; Henkelman, G. Improved Grid-Based Algorithm for Bader Charge Allocation. *J Comput Chem* **2007**, *28*, 899–908, doi:10.1002/jcc.20575.

77. Tang, W.; Sanville, E.; Henkelman, G. A Grid-Based Bader Analysis Algorithm without Lattice Bias. *Journal of Physics: Condensed Matter* **2009**, *21*, 084204, doi:10.1088/0953-8984/21/8/084204.

78. Friuli, V.; Bruni, G.; Musitelli, G.; Conte, U.; Maggi, L. Influence of Dissolution Media and Presence of Alcohol on the In Vitro Performance of Pharmaceutical Products Containing an Insoluble Drug. *J Pharm Sci* **2018**, *107*, 507–511, doi:10.1016/j.xphs.2017.06.001.

79. Esposito, S.; Silvestri, B.; Russo, V.; Bonelli, B.; Manzoli, M.; Deorsola, F.A.; Vergara, A.; Aronne, A.; Di Serio, M. Self-Activating Catalyst for Glucose Hydrogenation in the Aqueous Phase under Mild Conditions. *ACS Catal* **2019**, *9*, 3426–3436, doi:10.1021/acscatal.8b04710.

80. Esposito, S. Evolution of Sol–Gel Chemistry. In *Sol-Gel Synthesis Strategies for Tailored Catalytic Materials*; Springer International Publishing: Cham, 2023; pp. 43–51 ISBN 978-3-031-20722-8, https://doi.org/10.1007/978-3-031-20723-5_5.

81. Bonelli, B.; Tammaro, O.; Martinovic, F.; Nasi, R.; Dell'Agli, G.; Rivolo, P.; Giorgis, F.; Ditaranto, N.; Deorsola, F.A.; Esposito, S. Reverse Micelle Strategy for the Synthesis of MnO_x–TiO_2 Active Catalysts for NH_3 -Selective Catalytic Reduction of NO_x at Both Low Temperature and Low Mn Content. *ACS Omega* **2021**, *6*, 24562–24574, doi:10.1021/acsomega.1c03153.

82. Nasi, R.; Esposito, S.; Freyria, F.; Armandi, M.; Gadhi, T.; Hernandez, S.; Rivolo, P.; Ditaranto, N.; Bonelli, B. Application of Reverse Micelle Sol–Gel Synthesis for Bulk Doping and Heteroatoms

Surface Enrichment in Mo-Doped TiO2 Nanoparticles. *Materials* **2019**, *12*, 937, doi:10.3390/ma12060937.

83. Mancuso, A.; Blangetti, N.; Sacco, O.; Freyria, F.S.; Bonelli, B.; Esposito, S.; Sannino, D.; Vaiano, V. Photocatalytic Degradation of Crystal Violet Dye under Visible Light by Fe-Doped TiO2 Prepared by Reverse-Micelle Sol–Gel Method. *Nanomaterials* **2023**, *13*, 270, doi:10.3390/nano13020270.

84. Esposito, S. Synthetic Strategies for (Supported) Metal and Metal Oxide Catalysts: Case Studies. In *Sol-Gel Synthesis Strategies for Tailored Catalytic Materials*; 2023; pp. 53–71, https://doi.org/10.1007/978-3-031-20723-5_6.

85. Malik, M.A.; Wani, M.Y.; Hashim, M.A. Microemulsion Method: A Novel Route to Synthesize Organic and Inorganic Nanomaterials. *Arabian Journal of Chemistry* **2012**, *5*, 397–417, doi:10.1016/j.arabjc.2010.09.027.

86. Water in and around Micelles, Reverse Micelles, and Microemulsions. In *Water in Biological and Chemical Processes*; Cambridge University Press, 2013; pp. 261–276.

87. Choudhury, B.; Chetri, P.; Choudhury, A. Oxygen Defects and Formation of Ce^{3+} Affecting the Photocatalytic Performance of CeO_2 Nanoparticles. *RSC Adv.* **2014**, *4*, 4663–4671, doi:10.1039/C3RA44603D.

88. Shih, S.-J.; Wu, Y.-Y.; Chen, C.-Y.; Yu, C.-Y. Morphology and Formation Mechanism of Ceria Nanoparticles by Spray Pyrolysis. *Journal of Nanoparticle Research* **2012**, *14*, 879, doi:10.1007/s11051-012-0879-4.

89. Anghel, E.M.; Petrescu, S.; Mocioiu, O.C.; Cusu, J.P.; Atkinson, I. Influence of Ceria Addition on Crystallization Behavior and Properties of Mesoporous Bioactive Glasses in the SiO2–CaO–P2O5–CeO2 System. *Gels* **2022**, *8*, 344, doi:10.3390/gels8060344.

90. Woan, K.; Tsai, Y.-Y.; Sigmund, W. Synthesis and Characterization of Luminescent Cerium Oxide Nanoparticles. *Nanomedicine* **2010**, *5*, 233–242, doi:10.2217/nnm.09.106.

91. Schmitt, R.; Nenning, A.; Kraynis, O.; Korobko, R.; Frenkel, A.I.; Lubomirsky, I.; Haile, S.M.; Rupp, J.L.M. A Review of Defect Structure and Chemistry in Ceria and Its Solid Solutions. *Chem Soc Rev* **2020**, *49*, 554–592, doi:10.1039/C9CS00588A.

92. Luo, S.; Li, M.; Fung, V.; Sumpter, B.G.; Liu, J.; Wu, Z.; Page, K. New Insights into the Bulk and Surface Defect Structures of Ceria Nanocrystals from Neutron Scattering Study. *Chemistry of Materials* **2021**, *33*, 3959–3970, doi:10.1021/acs.chemmater.1c00156.

93. Bao, H.; Qian, K.; Fang, J.; Huang, W. Fe-Doped CeO2 Solid Solutions: Substituting-Site Doping versus Interstitial-Site Doping, Bulk Doping versus Surface Doping. *Appl Surf Sci* **2017**, *414*, 131–139, doi:10.1016/j.apsusc.2017.04.018.

94. Li, G.; Smith, R.L.; Inomata, H. Synthesis of Nanoscale Ce 1-x Fe x O 2 Solid Solutions via a Low-Temperature Approach. *J Am Chem Soc* **2001**, doi:10.1021/ja016502.

95. Zhao, B.; Shao, Q.; Hao, L.; Zhang, L.; Liu, Z.; Zhang, B.; Ge, S.; Guo, Z. Yeast-Template Synthesized Fe-Doped Cerium Oxide Hollow Microspheres for Visible Photodegradation of Acid Orange 7. *J Colloid Interface Sci* **2018**, *511*, 39–47, doi:10.1016/j.jcis.2017.09.077.

96. Bao, H.; Chen, X.; Fang, J.; Jiang, Z.; Huang, W. Structure-Activity Relation of Fe2O3–CeO2 Composite Catalysts in CO Oxidation. *Catal Letters* **2008**, *125*, 160–167, doi:10.1007/s10562-008-9540-3.

97. Liu, H.; Wu, Y.; Liu, L.; Chu, B.; Qin, Z.; Jin, G.; Tong, Z.; Dong, L.; Li, B. Three-Dimensionally Ordered Macroporous Fe-Doped Ceria Catalyst with Enhanced Activity at a Wide Operating Temperature Window for Selective Catalytic Reduction of NOx. *Appl Surf Sci* **2019**, *498*, 143780, doi:10.1016/J.APSUSC.2019.143780.

98. Aragón, F.F.H.; Aquino, J.C.R.; Ramos, J.E.; Coaquira, J.A.H.; Gonzalez, I.; Macedo, W.A.A.; da Silva, S.W.; Morais, P.C. Fe-Doping Effects on the Structural, Vibrational, Magnetic, and Electronic Properties of Ceria Nanoparticles. *J Appl Phys* **2017**, *122*, doi:10.1063/1.4999457.

99. Martínez-Arias, A.; Fernández-García, M.; Salamanca, L.N.; Valenzuela, R.X.; Conesa, J.C.; Soria, J. Structural and Redox Properties of Ceria in Alumina-Supported Ceria Catalyst Supports. *J Phys Chem B* **2000**, *104*, 4038–4046, doi:10.1021/jp992796y.

100. SCHWIDDER, M.; KUMAR, M.; KLEMENTIEV, K.; POHL, M.; BRUCKNER, A.; GRUNERT, W. Selective Reduction of NO with Fe-ZSM-5 Catalysts of Low Fe ContentI. Relations between Active Site Structure and Catalytic Performance. *J Catal* **2005**, *231*, 314–330, doi:10.1016/j.jcat.2005.01.031.

101. Shafia, E.; Esposito, S.; Manzoli, M.; Chiesa, M.; Tiberto, P.; Barrera, G.; Menard, G.; Allia, P.; Freyria, F.S.; Garrone, E.; et al. Al/Fe Isomorphic Substitution versus Fe2O3 Clusters Formation in Fe-Doped Aluminosilicate Nanotubes (Imogolite). *Journal of Nanoparticle Research* **2015**, *17*, 336, doi:10.1007/s11051-015-3130-2.

102. Katta, L.; Thrimurthulu, G.; Reddy, B.M.; Muhler, M.; Grünert, W. Structural Characteristics and Catalytic Performance of Alumina-Supported Nanosized Ceria–Lanthana Solid Solutions. *Catal Sci Technol* **2011**, *1*, 1645, doi:10.1039/c1cy00312g.

103. Makuła, P.; Pacia, M.; Macyk, W. How To Correctly Determine the Band Gap Energy of Modified Semiconductor Photocatalysts Based on UV–Vis Spectra. *J Phys Chem Lett* **2018**, *9*, 6814–6817, doi:10.1021/acs.jpclett.8b02892.

104. George, S.; Pokhrel, S.; Ji, Z.; Henderson, B.L.; Xia, T.; Li, L.; Zink, J.I.; Nel, A.E.; Mädler, L. Role of Fe Doping in Tuning the Band Gap of TiO_2 for the Photo-Oxidation-Induced Cytotoxicity Paradigm. *J Am Chem Soc* **2011**, *133*, 11270–11278, doi:10.1021/ja202836s.

105. El-Hagary, M.; Shaaban, E.R.; Moustafa, S.H.; Gad, G.M.A. The Particle Size-Dependent Optical Band Gap and Magnetic Properties of Fe-Doped CeO2 Nanoparticles. *Solid State Sci* **2019**, *91*, 15–22, doi:10.1016/j.solidstatesciences.2019.03.005.

106. Dhannia, T.; Jayalekshmi, S.; Santhosh Kumar, M.C.; Prasada Rao, T.; Chandra Bose, A. Effect of Iron Doping and Annealing on Structural and Optical Properties of Cerium Oxide Nanocrystals. *Journal of Physics and Chemistry of Solids* **2010**, *71*, 1020–1025, doi:10.1016/j.jpcs.2010.04.011.

107. Yang, H.; Jia, L.; Zhang, Z.; Xu, B.; Zhang, Q.; Yuan, S.; Xiao, Y.; Nan, Z.; Zhang, M.; Zhang, Y.; et al. Enhanced Photocatalytic VOCs Degradation Performance on Fe-Doped Ceria under Visible Light. *Appl Mater Today* **2022**, *29*, 101651, doi:10.1016/j.apmt.2022.101651.

108. Spanier, J.E.; Robinson, R.D.; Zhang, F.; Chan, S.-W.; Herman, I.P. Size-Dependent Properties of CeO2−y Nanoparticles as Studied by Raman Scattering. *Phys Rev B* **2001**, *64*, 245407, doi:10.1103/PhysRevB.64.245407.

109. Wu, Z.; Li, M.; Howe, J.; Meyer, H.M.; Overbury, S.H. Probing Defect Sites on CeO_2 Nanocrystals with Well-Defined Surface Planes by Raman Spectroscopy and O_2 Adsorption. *Langmuir* **2010**, *26*, 16595–16606, doi:10.1021/la101723w.

110. Dohčević-Mitrović, Z.D.; Šćepanović, M.J.; Grujić-Brojčin, M.U.; Popović, Z.V.; Bošković, S.B.; Matović, B.M.; Zinkevich, M.V.; Aldinger, F. The Size and Strain Effects on the Raman Spectra of Ce1−xNdxO2−δ (0≤x≤0.25) Nanopowders. *Solid State Commun* **2006**, *137*, 387–390, doi:10.1016/j.ssc.2005.12.006.

111. Popović, Z. V.; Dohčević-Mitrović, Z.D.; Paunović, N.; Radović, M. Evidence of Charge Delocalization in Ce 1 − x Fe x 2 + (3 +) O 2 − y Nanocrystals (x = 0 , 0.06, 0.12). *Phys Rev B* **2012**, *85*, 014302, doi:10.1103/PhysRevB.85.014302.

112. Nakajima, A.; Yoshihara, A.; Ishigame, M. Defect-Induced Raman Spectra in Doped <math Display="inline"> <mrow> <msub> <mrow> <mi Mathvariant="normal">CeO</Mi> </Mrow> <mrow> <mn>2</Mn> </Mrow> </Msub> </Mrow> </Math>. *Phys Rev B* **1994**, *50*, 13297–13307, doi:10.1103/PhysRevB.50.13297.

113. Gallucci, N.; Hmoudah, M.; Martinez, E.; El-Qanni, A.; Di Serio, M.; Paduano, L.; Vitiello, G.; Russo, V. Photodegradation of Ibuprofen Using CeO2 Nanostructured Materials: Reaction Kinetics, Modeling, and Thermodynamics. *J Environ Chem Eng* **2022**, *10*, 107866, doi:10.1016/j.jece.2022.107866.

114. Paparazzo, E. Use and Mis-Use of x-Ray Photoemission Spectroscopy Ce3d Spectra of Ce_2O_3 and CeO_2. *Journal of Physics: Condensed Matter* **2018**, *30*, 343003, doi:10.1088/1361-648X/aad248.

115. Romeo, M.; Bak, K.; El Fallah, J.; Le Normand, F.; Hilaire, L. XPS Study of the Reduction of Cerium Dioxide. *Surface and Interface Analysis* **1993**, *20*, 508–512, doi:10.1002/sia.740200604.

116. Idriss, H. On the Wrong Assignment of the XPS O1s Signal at 531–532 EV Attributed to Oxygen Vacancies in Photo- and Electro-Catalysts for Water Splitting and Other Materials Applications. *Surf Sci* **2021**, *712*, 121894, doi:10.1016/j.susc.2021.121894.

117. Cardenas, L.; Molinet-Chinaglia, C.; Loridant, S. Unraveling Ce^{3+} Detection at the Surface of Ceria Nanopowders by UPS Analysis. *Physical Chemistry Chemical Physics* **2022**, *24*, 22815–22822, doi:10.1039/D2CP02736D.

118. Liu, T.; Guo, L.; Tao, Y.; Hu, T.D.; Xie, Y.N.; Zhang, J. Bondlength Alternation of Nanoparticles Fe2O3 Coated with Organic Surfactants Probed by EXAFS. *Nanostructured Materials* **1999**, *11*, 1329–1334, doi:10.1016/S0965-9773(99)00425-0.

119. Turco, R.; Bonelli, B.; Armandi, M.; Spiridigliozzi, L.; Dell'Agli, G.; Deorsola, F.A.; Esposito, S.; Di Serio, M. Active and Stable Ceria-Zirconia Supported Molybdenum Oxide Catalysts for Cyclooctene Epoxidation: Effect of the Preparation Procedure. *Catal Today* **2020**, *345*, 201–212, doi:10.1016/j.cattod.2019.10.036.

120. Wang, Y.; Wang, F.; Song, Q.; Xin, Q.; Xu, S.; Xu, J. Heterogeneous Ceria Catalyst with Water-Tolerant Lewis Acidic Sites for One-Pot Synthesis of 1,3-Diols via Prins Condensation and Hydrolysis Reactions. *J Am Chem Soc* **2013**, *135*, 1506–1515, doi:10.1021/ja310498c.

121. Rebellato, J.; Natile, M.M.; Glisenti, A. Influence of the Synthesis Procedure on the Properties and Reactivity of Nanostructured Ceria Powders. *Appl Catal A Gen* **2008**, *339*, 108–120, doi:10.1016/j.apcata.2007.12.031.

122. Badri, A.; Binet, C.; Lavalley, J.-C. An FTIR Study of Surface Ceria Hydroxy Groups during a Redox Process with H2. *Journal of the Chemical Society, Faraday Transactions* **1996**, *92*, 4669, doi:10.1039/ft9969204669.

123. Natile, M.M.; Boccaletti, G.; Glisenti, A. Properties and Reactivity of Nanostructured CeO_2 Powders: Comparison among Two Synthesis Procedures. *Chemistry of Materials* **2005**, *17*, 6272–6286, doi:10.1021/cm051352d.

124. Matussin, S.N.; Khan, F.; Harunsani, M.H.; Kim, Y.-M.; Khan, M.M. Visible-Light-Induced Photocatalytic and Photoantibacterial Activities of Co-Doped CeO_2. *ACS Omega* **2023**, *8*, 11868–11879, doi:10.1021/acsomega.2c07058.

125. Xu, B.; Yang, H.; Zhang, Q.; Yuan, S.; Xie, A.; Zhang, M.; Ohno, T. Design and Synthesis of Sm, Y, La and Nd-doped CeO_2 with a Broom-like Hierarchical Structure: A Photocatalyst with Enhanced Oxidation Performance. *ChemCatChem* **2020**, *12*, 2638–2646, doi:10.1002/cctc.201902309.

126. Zdanowicz, T.; Rodziewicz, T.; Zabkowska-Waclawek, M. Theoretical Analysis of the Optimum Energy Band Gap of Semiconductors for Fabrication of Solar Cells for Applications in Higher Latitudes Locations. *Solar Energy Materials and Solar Cells* **2005**, *87*, 757–769, doi:10.1016/j.solmat.2004.07.049.

127. Rao, Y.; Xue, D.; Pan, H.; Feng, J.; Li, Y. Degradation of Ibuprofen by a Synergistic UV/Fe(III)/Oxone Process. *Chemical Engineering Journal* **2016**, *283*, 65–75, doi:10.1016/j.cej.2015.07.057.

Highlights

- Reverse micelle synthesis fosters Fe doping of nanocrystalline CeO_2
- 2.5 mol % iron-doped ceria leads to high charge delocalization
- Efficient visible-light photodegradation of ibuprofen with 2.5 mol % Fe-CeO_2
- Substitutional Fe favours the oxygen vacancies formation and ibuprofen adsorption.
- The by-product of the ibuprofen degradation is 1-ethenyl-4-(2-methylpropyl)benzene.